Localized Programmable Gas Phase Electrodeposition Yielding Functional Nanostructured Materials and Molecular Arrays

A DISSERTATION
SUBMITTED TO THE FACULTY OF THE GRADUATE SCHOOL
OF THE UNIVERSITY OF MINNESOTA
BY

En-Chiang Lin

IN PARTIAL FULFILLMENT OF THE REQUIREMENTS
FOR THE DEGREE OF
DOCTOR OF PHILOSOPHY

Advisor: Heiko O. Jacobs

April 2013

Acknowledgments

The pursuit of a PhD in Electrical Engineering at the University of Minnesota has been a great challenge over the past five years. I would not have been able to complete this journey without the aid and support of countless people. While I am thankful to everyone who has helped me through the unfamiliar concepts and the late nights of experiments, there are some specific individuals whose contributions have been particularly significant.

I thank my doctoral advisor Prof. Heiko O. Jacobs for guiding my research over the entirety of graduate school. I have acquired a great deal of both knowledge and skill under his guidance. First and foremost Prof. Jacobs taught me how to conduct exploratory research in a professional setting. He also continually challenged me by regularly looking at results from a unique perspective and by finishing experimental setups using existing tools. I would also like to thank my doctoral committee members, Prof. Mo Li, Prof. Sang-Hyun Oh, and Prof. Rusen Yang for their time and effort in reviewing this work.

I would like to thank past and present Jacobs´ group members including Chad Barry, Xinyu Wang, Robert Knuesel, Jesse Cole, Shameek Bose, Chris Smith, Yu Chen, Sechul Park, Michael Motala, Jun Fang, and Forrest Johnson. Bouncing ideas off of interested coworkers has been an enjoyable part of my graduate career.

Last but not least, I owe my greatest gratitude to my beloved parents and my wife who had supported me to begin this journey. And as the burden grew, they never ceased to give me assurance that I can and I will finish this journey.

Abstract

This thesis focuses on nanomanufacturing processes for the heterogeneous integration of nanomaterials and molecules. We demonstrate and discovered a novel gas phase method to control material flux at specific points on a surface which is based on the interplay of high mobility gas ions and lower mobility nanoparticles and molecules in the presence of a patterned substrate. The thesis is divided into two parts describing applications of the discovered process for the localized deposition of

(A) metallic and semiconducting particles producing functional nanostructured deposits including multimaterial sensor arrays and nanostructured electrodes for photovoltaic applications and,

(B) molecules for gas sensor application demonstrating improved collection efficiencies and sensitivity over previously methods.

Section (A) begins with the description of an arc discharge based method to produce a flux of charged nanoparticles (<5nm particles Au, Ag, Pt, W, TiO_2, ZnO and Ge) which are characterized using various methods. It then describes a process to locally deposit the charged particles into extended two and three dimensional metallic and semiconducting nanostructured deposits. The thesis describes the use externally-biased electrodes to achieve an electronic shutter to turn ON/OFF the deposition in selected domains. Subsequently it explores and describes the use of patterned dielectrics whereby the patterned dielectrics are charged to define arrays of electrodynamic lenses. Incorporation of these lensing structures was found to enable nanostructured deposits with sub 100nm lateral resolution. The utility of the discovered processes are demonstrated in two areas. For the first application, semiconducting nanomaterial are sequentially deposited on the same substrate to fabricate a multi-material / multi-functional sensor array on a single substrate in a single deposition process. The process eliminates critical alignment and masking steps and has a higher material efficiency when compared with traditional vapor deposition methods. In the second application, we demonstrate the fabrication of 3D nanostructured electrodes for photovoltaic application. The second application adjusts the material flux in selected domains to identify nanostructures and device metrics in a combinatorial way.

Section (B) applies the process to the localized collection of airborne molecules. The goal was to determine if the process can be scaled to particles with molecular dimensions. This turned out to be the case. As an application we demonstrate enhanced collection efficiencies of molecular species in gas sensor applications. The research recognizes that various nanostructured sensor designs currently aim to achieve or claim single molecular detection by a reduction of the active sensor size. However, a reduction of the sensor size has the negative effect of reducing the capture probability considering the diffusion based analyte transport commonly used. Specifically, we applied the discovered localized programmable electrodynamic precipitation concept to collect, spot, and detect airborne species in an active-matrix array-like fashion. The method is tested using surface enhanced Raman spectroscopy (SERS). The process can produce hybrid molecular arrays on a single chip over a broad range of molecular weights including small molecules or large macromolecules. From a gas sensor system point of view it was possible to improved collection efficiencies and sensitivity over previously method.

Table of Contents

List of Tables

CHAPTER IV

List of Figures

CHAPTER I

CHAPTER III

CHAPTER IV

CHAPTER V

CHAPTER VI

Chapter I

Motivation, Background and Project Introductions

Motivation

Nanomaterials, the building blocks of future nanotechnological devices, are most commonly fabricated using solution chemistry or gas phase chemistry and can provide a variety of functions. The use of nanomaterials as building blocks, however, requires novel deposition methods to enable the creation of functional devices and systems. The primary objective of this thesis is to develop nanomanufacturing processes to synthesize and integrate inorganic nanomaterials with control over location, diameter, length, and geometrical orientation. Additionally, this thesis also proposes and experimentally demonstrates a programmable localized electrodynamic precipitation concept to collect, spot, and detect airborne species in an active-matrix array-like fashion.

General Background

Inorganic nanomaterials in form of nanoparticles and nanowires have attracted attention due to their unusual properties including quantum size effects, high surface area to volume ratio, and increased catalytic activity to name a few. These properties have influenced almost any research discipline in recent years including the fields of printable electronics, optoelectronics, physical sensors, solar cells, biological screening, and environmental protection[1-5]. Today there are a host of synthesis techniques available to form the desired inorganic nanomaterials which can be grouped into two classes: low temperature wet chemical and high temperature gas/vapor phase methods. Gas/vapor phase methods such as thermal flow synthesis[6-8], laser ablation[9], sputtering[10], plasma induced synthesis[11], and arc discharge[12, 13] can produce various types of nanoparticles and nanowires including high temperature and high performance semiconductors that are difficult to make using low temperature wet chemical methods. Among the high temperature gas phase methods, the atmospheric pressure arc discharge method distinguishes itself since the high temperature arc discharge region is surrounded by a low temperature deposition region that is compatible with deposition on flexible

plastic substrates. Atmospheric pressure operation supports a higher mass flow rate when compared to vacuum deposition systems and inexpensive production setups while maintaining the ability to produce and deposit a wide selection of materials including metals and semiconductors[12, 13] in a single reactor system.

A challenge today can be found in the design of gas phase systems that combine high temperature synthesis with low temperature local area deposition on foreign substrates for printable electronics applications. Selected area deposition schemes are well established in the liquid phase but remain largely absent in the gas phase. Current direct write gas-phase deposition methods use nozzles or aerodynamic streams[14, 15] to deposit the materials locally in a serial fashion with 30 µm resolution.

Selected area deposition has also been reported using pre-patterned surfaces. For example, it has been demonstrated that charge patterned insulators can be used to attract a limited amount of oppositely charged particles[16, 17] with <100 nm resolution. While pre-patterned surfaces provided much higher resolution they remained limited to 2-dimensional deposits of a few monolayer thicknesses (Figure 1-1). The use of pre-patterned surfaces had the additional disadvantage that materials could not be altered to vary across the substrate. Very high resolution but mono-material and two-dimensional prints have been the state of the art using pre-patterned surfaces.

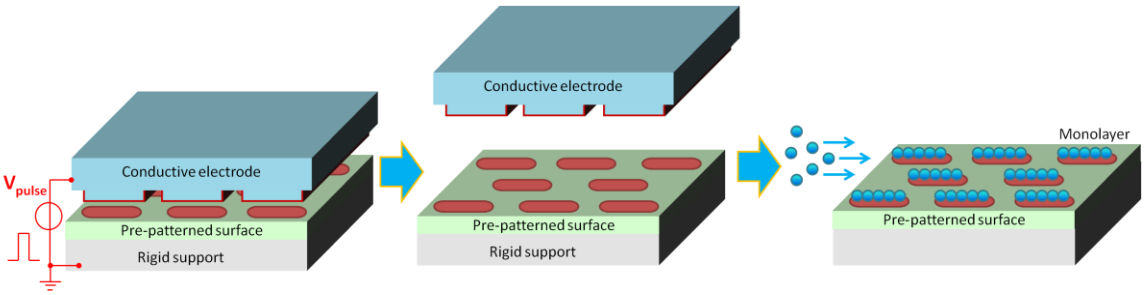

Fig. 1-1: Selected area deposition using conventional nanoxerography is limited to 2D prints. It uses trapped charges inside a continuous insulator (red area) which can only attract a limited amount of charged material. Particle deposition will eventually lead to the screening of the trapped charge which will terminate the deposition.

Section A – Gas Phase Electrodeposition (Publications 1 and 2)

of metallic and semiconducting particles producing functional two and three dimensional nanostructured deposits and applications as multimaterial sensor arrays and nanostructured electrodes for photovoltaic applications.

Introduction (Section A): At the outset of this research we had a number of goals. One goal was to find a localized gas phase deposition concept that builds on previous knowledge in the research group of Prof. Jacobs who pioneered NanoXerographic Printers[2, 16, 18-20]. NanoXerography uses a charged dielectric which attracts oppositely charged nanoparticles at a lateral resolution that exceeds conventional Xerographic printers by 3 orders of magnitude. While extremely high lateral resolution (<100 nm) had already been demonstrated the process had not yet found a widespread use. The goal was to build on the basic physical understanding while looking at alternative designs and systems that would provide a greater applicability. The following challenges and limitations were known:

1. Prior Nanoxerogaphic methods used a locally charged continuous dielectric which could only attract a limit amount of oppositely charged material.
2. The prints were limited to be unimaterial (monochrome) and it was not possible to deposit more than one material type onto desired areas.
3. The prints were limited to be two-dimensional and an extension into the third dimension appeared unattainable.
4. The range of nanoparticles was fairly limited both in terms of size (>50 nm) and type (Ge, Ag, and Au).

Five years later we have developed a deposition system which eliminated the limitation that the deposits could only be a few monolayers thick. We introduced a concept that provides localized charge dissipation and replenishing of the charge differentials. We extended the process to more materials enabling multi material deposition. The process can now alter both the material amount and the material type on the substrate which has found an application in the combinatory discovery of nanostructured devices testing

various combinations on a single substrate in a single experiment. We have extended the process into the third dimension. At present we are able to control the flux of charged material to locations with sub 100 nm lateral resolution to form bridges and interconnects in selected domains or, in the simplest case, to form straight metallic nanowire arrays whose height and density are adjusted to vary across the substrate. We have also extended the range of the materials. The dimensions of the primary particles has been reduced from 50 nm to molecular (<1 nm) dimensions. The process has little similarities with what we used at the outset. It has grown into a different system. It is no longer called Nanoxerography but "Gas Phase Electrodeposition" since it shares more commonalities with electrodeposition in the liquid phase.

Figure 1-2 provides an illustration to introduce the basic features of the "Gas Phase Electrodeposition" process that will be further described in detail in the respective publications[21-23] and section A of this thesis. In brief the process incorporates *(i)* particle generation, *(ii)* charging, and *(iii)* selected area deposition within a single compact apparatus. Electrons generated in the plasma region are accelerated by the applied electric field to the anode, producing gas ions (G+) through impact ionization. The gas ions (G+) move and impact the cathode which leads to cathode erosion. *(ii)* The eroded material (M) leaves the cathode that is surrounded by a positive (G+) space charge region and picks up positive charge resulting in the depicted (M+) particle; negative and neutral particles will be present as well. *(iii)* Selected area deposition is possible since all charged species are influenced by nearby electrodes. Depicted is the case for a negatively-biased (V_d <0) domain. The deposition process should be considered as an electrodynamic process since the field distribution evolves over time. Mass and electrical mobility of the involved species is important. The depicted gas ions (G+) have a higher electrical mobility than the heavier metal particle. On a time scale and in the initial stages of the experiments the gas ions (G+) arrive at the sample surface first, which results in the depicted sheath of space charge (G+) on the sample surface and alters the potential distribution. Under equilibrium conditions a flux of positive material is established which flows to the conducting and bare electrode sites. Compared to patterning by traditional photolithography, no liftoff is required and less material is lost as a result.

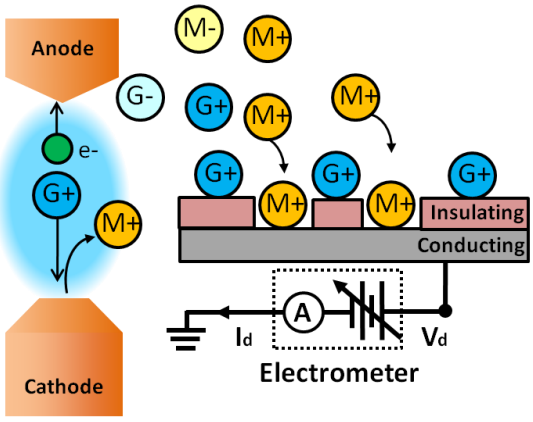

Fig. 1-2: Basic concept depicting the production of charged nanomaterials by cathode erosion and ionization inside the plasma region whereby material flux is diverted towards the biased substrate leading to a measurable substrate current I_d; I_d reflects the rate of charge deposition and dissipation on the substrate.

Summary of Main Results (Section A): A gas phase deposition system to deposit material into addressable areas forming vias, interconnects, patterned multimaterial or multilayer films in a programmable fashion is demonstrated. Such a deposition process would be important in the context of printable electronics since many functional nanomaterials are presently formed in the gas phase. Additionally, this printing concept is also extended to a multi material deposition scheme demonstrating three-dimensional nanostructured deposits which are applied in the combinatory discovery of nanostructured devices. Specifically, we report a multi-material selected area deposition process that produces <5 nm nanoparticles of Pt, Ag and W, which are subsequently deposited into photoresist openings with sub 100 nm lateral resolutions and aspect ratios of 10. We demonstrate multimaterial nanostructures containing sections of Pt, Ag and W, whereas individual thickness, density, and height is varied and the sequence of the material is switched and selected to be different from one domain to the next. The reported gas phase process shares some of the characteristics of electrodeposition in the liquid phase. The process allows us to control the flux of charged material to locations with 100 nm lateral resolution to form bridges and interconnects in selected domains or, in the simplest case, to form straight metallic nanowire arrays whose height and density are adjusted to vary across the substrate.

This reported process can be applied to the combinatorial screening of various types of nanostructured deposits for electronic and optoelectronic device applications/discovery. As a first demonstration in this direction we test whether the tool can be used to identify/discover electrode designs that improve the carrier extraction efficiencies of bulk heterojunction photovoltaic cells. The approach discussed here does not use mechanical shutters to turn ON/OFF deposition in certain areas and provides programmability with much higher resolution and feature density than prior concepts that have been applied to the fields of optoelectronics and photovoltaics[24-27]. We explored different interpenetrating electrode designs in particular 3D nanowire-based electrode arrays where height and density were adjusted from one domain to the next. The protocol varied pitch from 3 μm to 5 μm and height from 500 nm to 900 nm to explore the impact on absorption efficiency (η_A) and minority carrier extraction efficiency (η_{ED}). The completed solar cell domains share the same substrate, processing, and testing conditions. Short circuit current densities ranged from 7.7 to 12.2 mA/cm^2. The relative power conversion efficiencies (PCE) increased by 47% in domains that carried dense nanowire arrays when compared to the flat reference on the same substrate.

Programmable selected area deposition of dissimilar materials is also used to fabricate physical sensor arrays containing light and humidity sensitive areas on the same chip. The physics of how the particles are charged in the particular arc discharge system prior to deposition on a substrate at room temperature is discussed. It involves diffusional charging through a positive space charge region surrounding the electrode that is consumed by the process forming charged nanocusters which finally deposit on a low temperature substrate.

Section B- Electrostatic Precipitation (Publications 3 and 4)

of Molecules enabling collection, spotting, and detection of airborne species in an active-matrix array like fashion.

Introduction (Section B): In section A we learned that we could guide nanoparticles to precise points in space with very high resolution and collection efficiencies. The natural question was if it would be possible to do this with molecules as well which leads to section B of the thesis. Section B was not planned at the outset of the research but evolved naturally as we gained a deeper understanding of the underlying processes; it was curiosity driven. For example, we wanted to know if it is possible to use an electrodynamic nanolens to guide the deposition of molecules to precise points in space. The problem was that the molecules would be too small to be directly visualized and we had to think about advanced sensing means to provide evidence that guided deposition would be possible. In the end this turned out to be the case which led to a new application where localized molecular collection is used to enhance the sensitive of various gas sensors. The research recognizes that various nanostructured sensor designs currently aim to achieve or claim single molecular detection by a reduction of the active sensor size. However, a reduction of the sensor size has the negative effect of reducing the capture probability considering the diffusion based analyte transport commonly used. This is where a localized delivery concept could be used to collect, spot, and detect airborne species in an active-matrix array like fashion.

The broader context and background of this research is that the detection of small molecules and airborne species at low concentration commonly requires sensing schemes where the analytes are absorbed on a surface. The process of absorption and precipitation is therefore critical to the detection limit of the analytes. This is true for all established gas phase sensing concepts including gas chromatography[28], ion mobility spectrometry (IMS)[29, 30], mass spectrometry[31], metal-semiconductor-metal-based sensors[32-34], chemical field effect transistors[35], nanocantilever[36], infrared detection[37], and surface enhanced Raman spectroscopy (SERS)[38, 39]. Interestingly most of the more recently reported sensing schemes aim at increasing the sensitivity to a single molecular level[40] and use diffusion as a mechanism for transport which leads to a collection

efficiency of the airborne species which is not optimized. In other words, single molecular detection sensitivity is important but requires the molecule of interest to reach the sensing surface with maybe sub 100 nm in size. Effective collection on a small sensing area is not possible based on diffusion alone and the employment of a directed force will be required to solve the problem of transport. Both the thermophoretic and Coulomb force can be utilized to transport the analytes from a distance away to the sensing surface. At practical temperature gradients the thermophoretic force, however, remains low compared to concepts that use electrostatic precipitation[41]. Different from prior methods[28-33, 35-39] section B investigates the use of programmable localized electrodynamic force fields to collect, spot, and detect airborne species in an active-matrix array like fashion. The approach presented in section B does not use mechanical masks[42, 43] or high-precision contact-printing robots[44, 45] to deliver the analytes to desired points and provides programmability with a lateral resolution that is several orders of magnitudes higher. Molecules of one type are directed from a space that is centimeters away to specific sensing regions and areas with 100 nm control over the lateral position and spot size. As an example, in one of the discussed cases we compared a diffusion based analyte deliver with an electrodynamic approach that incorporated a nanolense design. The nanolens based process was able to detect charged benzenethiol molecules at an estimated level of 1.5 ppb (parts per billion) within 10 s; as a comparison, to detect uncharged molecules using a standard mechanism of diffusion a concentration of 6 ppm (parts per million) is required.

Summary of Main Results (Section B):

Publications 3 demonstrate a localized electrodynamic precipitation concept to collect, spot, and detect airborne species. Molecules are directed from a space that is centimeters away to specific sensing regions and areas with 100 nm control over the lateral position and spot size. The detection scheme is demonstrated using a surface-enhanced Raman spectroscopy (SERS) sensitized nanostructured surface including the standardized “Ag film over Nanosphere (AgFON) substrate”[38, 46]. The result is that SERS signals is enhanced by a factor of 615 comparing identical sensor surfaces. The process is able to detect charged benzenethiol molecules at an estimated level of 1.5 ppb

(parts per billion) within 10s; as a comparison, to detect uncharged molecules using a standard mechanism of diffusion a concentration of 6 ppm (parts per million) is required. Moreover, the reported process is applied to produce hybrid molecular arrays on a single chip over a broad range of molecular weights including small molecules such as benzenethiol (110.18 Dalton) and 4-fluorobenzenethiol (128.17 Dalton) or large macromolecules such anti-mouse IgG proteins (~150k Dalton).

Publication 4 compares three different analyte delivery concepts (standard diffusion, global electrodynamic precipitation, and localized nanolens based precipitation) and three different SERS enhancement layers (a flat silver film, a nanolens enabled localized deposited film of silver nanoparticles, and the standard AgFON surface layer) on a single chip. The nanolens array enables us to funnel and concentrate the airborne analyte molecules to discrete sensing points with sub 100 nm lateral resolution. The introduction of this concept had the biggest impact in terms of increasing the SERS signal intensity; a factor of 633 when compared to a standard mechanism of diffusion was observed. The nanolens array was also used to direct the precipitation of Ag nanoparticles to prepare a SERS enhancement layer which performed equally well as the (AgFON) standard.

Chapter II

Introductory Note

For the Set of Four Articles

The following chapters present four articles that have been published or are in print in pair reviewed journals with the exception of article 4 which has been submitted:

Chapter III (Publication 1, published) addresses semiconductor nanoparticle synthesis and integration out of the gas phase.

Chapter IV (Publication 2, published) addresses arc discharge synthesis and continuous metal nanocluster deposition from the gas phase.

Chapter V (Publication 3, in print) addresses a localized programmable electrodynamic precipitation concept to collect, spot, and detect airborne species in an active-matrix array like fashion.

Chapter VI (Publication 4, submitted) addresses a localized programmable electrodynamic precipitation concept to collect, spot, and detect airborne species in an active-matrix array like fashion adding more domains and a feature of localized nanoparticle deposition to enable an in-situ fabrication of the sensor surface.

Chapter III

Mimicking Electrodeposition in the Gas Phase: a Programmable Concept for Selected Area Fabrication of Multimaterial Nanostructures

Jesse J. Cole*, En-Chiang Lin*, Chad R. Barry, and Heiko O. Jacobs

* These authors contributed equally to this work.

Reproduced with permission from:

Small 6(10), 1117-1124 (2010)

3.1 Introduction

Modern interest in nanotechnology as a platform for functional systems drives the need for techniques to localize deposition of metals, oxides, and semiconducting materials. From a synthesis point of view, these materials are commonly formed in the liquid or gas phase. One of the most powerful liquid phase techniques remains traditional electrodeposition which has several unique characteristics absent from emerging direct write[47-49] or transfer techniques[50]. The most important being the ability to locally program the deposition of material (ions[51], nanoparticles[52, 53], and nanowires[54]) by simply applying a bias to an electrode. This characteristic supports programmable selected area deposition for materials and is presently limited to the liquid phase. The closest known gas phase extension to electrodeposition are electrostatic precipitators[55] which employ electrically biased plates to attract charged particles for filter applications. A gas phase deposition system to deposit material into addressable areas forming vias, interconnects, patterned multimaterial or multilayer films in a programmable fashion has, however, not yet been reported. Such a deposition process would be important in the context of printable electronics since many functional nanomaterials are presently formed in the gas phase. The present report describes a system working at atmospheric pressure to form electrically interconnected nanostructured thin films with 60nm lateral resolution and predetermined thickness. The system uses a DC plasma arc discharge between two consumable electrodes as a material source. The use of a DC arc discharge between consumable electrodes is a known concept to produce charged nanomaterials in large quantities; DC arc discharge between graphite electrodes led to the discovery and industrial production of fullerenes and carbon nanotubes[56-59] and the concept has also been extended to produce GaN[60], Pd[61], and Si[62] clusters and particles to name a few. In these earlier systems, particles coated the reactor walls uniformly.

Here we describe an insitu method which couples the particle source with a localized deposition system to mimicking electrodeposition in a gaseous environment. The approach uses a patterned substrate to funnel the material to specific locations with 60nm standard deviation in positional accuracy and uses an array of electrically biased domains to sequentially program the deposition of more than one material type. This is different from prior work in the field of gas phase nanoxerography where nanoparticles were

deposited onto charged substrate locations using a fixed amount of initial charge inside a dielectric[18] or a PN junction[63]. These prior methods do not allow programming. Moreover the fixed amount of initial charges limits the quantity of charged material that can be attracted before the trapped charges are depleted and screened. In the present case the biased electrodes provide a path for charge neutralization and maintain a constant potential difference that directs the assembly until the external voltage is turned off. This provides control over the amount of material and the type of material that can be deposited onto a desired area. As an application programmable selected area deposition of dissimilar materials is used to fabricate physical sensor arrays containing light and humidity sensitive areas on the same chip. The physics of how the particles are charged in the particular arc discharge system prior to deposition on a substrate at room temperature is discussed and involves diffusional charging through a positive space charge region surrounding the electrode that is consumed by the process forming charged nanoclusters which finally deposit on a low temperature substrate.

3.2 Results and Discussion

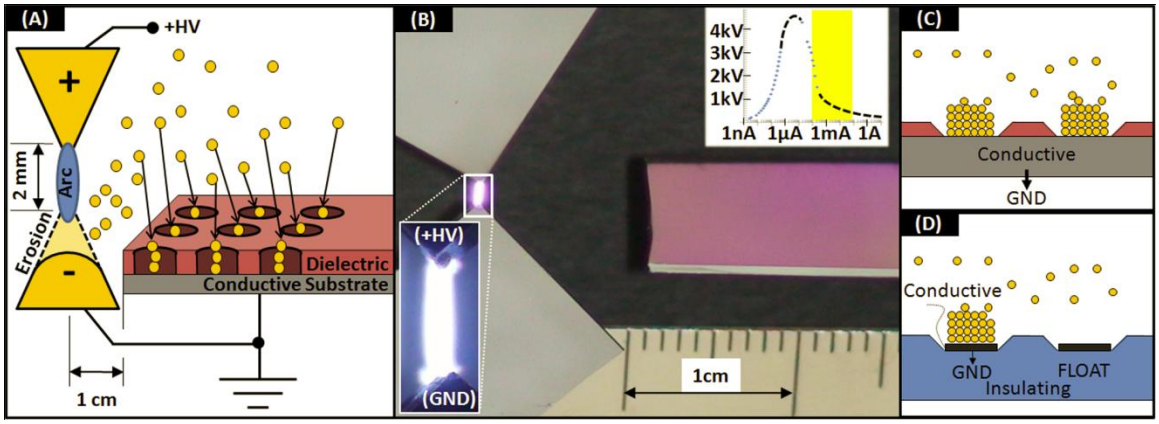

Figure 3-1. *Schematic and photograph of the basic elements of the prototype gas phase nanocluster electrodeposition system. (A) An atmospheric pressure DC arc discharge is established between two consumable electrodes that are separated by 2 mm. (B and zoom) The photograph shows the typical appearance of the arc between silicon electrodes where the cathode at the bottom initially sharp is rounded and consumed over time. (B inset) The arc is operated within the negative differential resistance regime highlighted in the recorded I/V characteristic which is accomplished using a current*

controlled high voltage source as opposed to the positive differential resistance corona discharge region to the left. Produced nanoparticles are collected on a grounded substrate outside the plasma region. (C) The grounded conductive substrate can be partially shielded using a patterned dielectric to accomplish focused assembly into the openings or (D) segmented into separated programmable regions.

Figure 3-1 illustrates the basic elements and dimensions of the apparatus. It uses a 0.1-100 mA DC plasma arc discharge between two consumable electrodes (left side of A, B) to continuously generate nanoparticles and a third sample electrode placed in the region outside of the visible plasma volume (aerosol region) to collect 20 nm Au, 15 nm Si, 15 nm TiO_2, 15 nm ZnO, or 10 nm Ge nanoparticles (right side of A, B). Nanoparticle collection is discussed later in Figure 3-3 (schematic C) and Figure 3-5 (schematic D). Additional details for the apparatus used here are included in the Experimental section. The anode (B, top electrode) was given a high positive potential and the cathode (B, bottom) was electrically grounded. The upper right inset in Figure 1B shows a typical current voltage (I/V) arc characteristic for Si electrodes with 2 mm gap distance. We operated the system in the arc regime to the right that is characterized by the negative differential resistance as opposed to corona regime to the left. Photographs of the arc (B inset) were taken at 10x reduced arc power (1mA, 1kV, and 1W) in order to resolve the electrode showing the expected blue-white arc luminescence for atmospheric pressure air conditions (21% O_2 and 78% N_2 by mole) and red-purple arc luminescence (not shown) after argon purge (>99.9% Ar). Arc luminescence indicates positive ionization of gas species.[64] The process of nanoparticle formation using atmospheric pressure arcs is well established and we refer to Smirnov[65] for an introduction. In brief high mobility electrons generated by the arc are accelerated by the applied electric field to the anode, producing gas ions as they travel. Incident positive gas ions are brought to the cathode where they impact the cathode tip surface. Erosion is observed only at the cathode because the heavy positive gas ions will release more kinetic energy than the electrons when impacting the electrode surface. The erosion process increases with the arc current.[66]

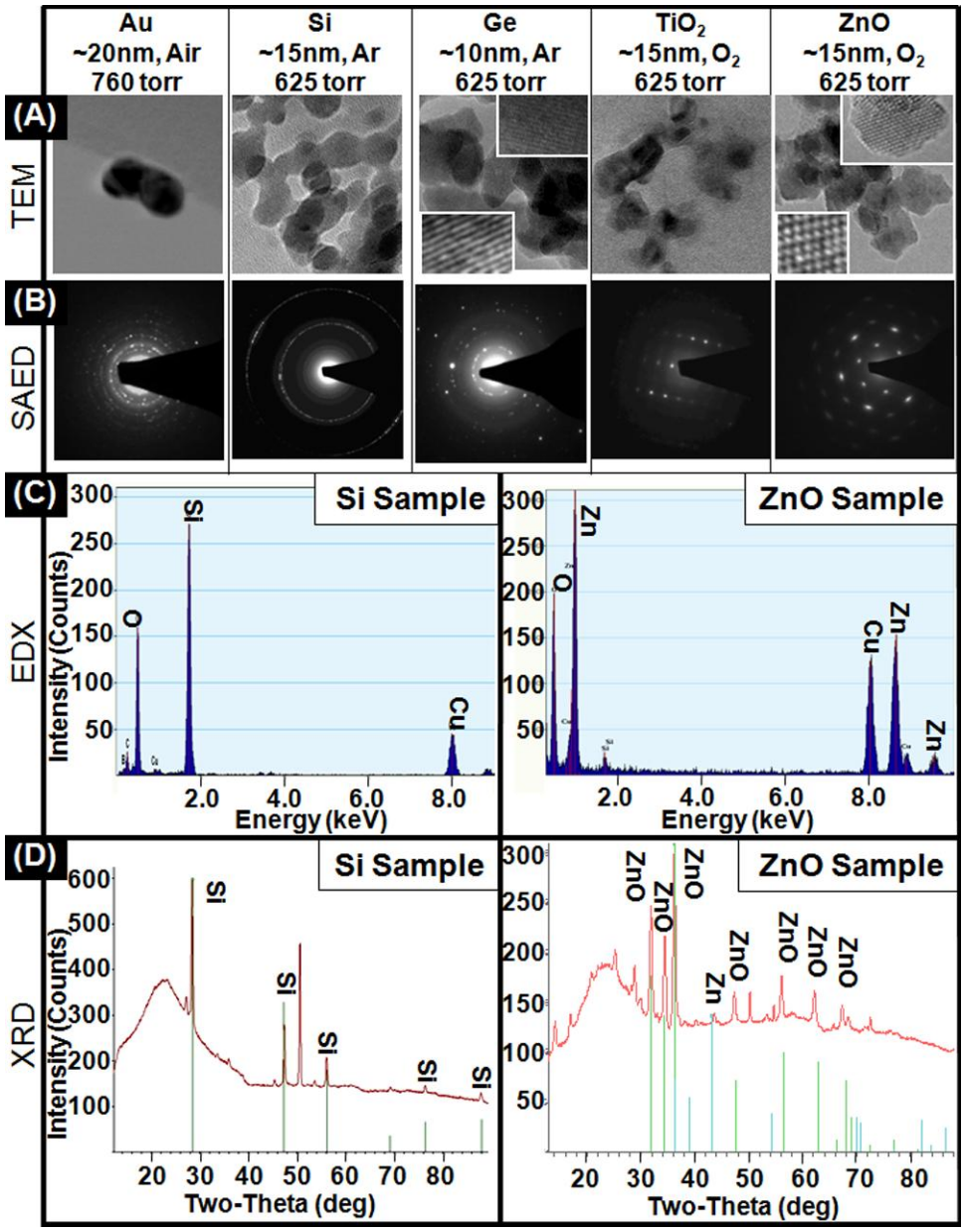

Figure 3-2. *Characterization of nanomaterials produced by atmospheric pressure arc discharge. (A) TEM results show that sub-20nm nanoparticles of Au, Si, Ge, TiO_2 and ZnO were generated, with HRTEM images (A insets) showing fringes for Ge and ZnO particles. (B) SAED confirms high particle crystallinity in all cases. (C) EDX results for Si and ZnO suggest the nanoparticle material type was related to the arc electrode material with a noticeable oxygen presence in its surface sensitive signal. (D) XRD data confirms strong unoxidized Si peaks suggesting minimal oxidation of Si nanoparticle interiors which contrasts the nearly complete oxidation of Zn into ZnO.*

Figure 3-2 provides material specific data to represent a few of the nanomaterials that are formed as a result of cathode erosion at an input power that was limited to 10W to prevent rapid evaporation of the cathodes. The results confirm that DC arc discharge can quickly be adapted to produce a variety of materials which are considered important in the field of printable electronics. The average particle sizes were found to be 20 nm for Au, 15 nm for Si, 10nm for Ge, 15nm for TiO_2, and 15nm for ZnO. EDX (Energy Dispersive X-ray Spectroscopy) for Si and ZnO nanoparticles shows the presence of oxygen in addition to the electrode material. The XRD (X-ray Diffraction) which is sensitive to material deeper than the surface shows strong Si peaks and absence of any significant SiO_2 suggesting that the Si particles have crystalline Si cores with SiO_2 surfaces. This contrasts the case when Zn electrodes where used; here XRD suggests nearly complete oxidation forming ZnO in the semiconducting zincite form.

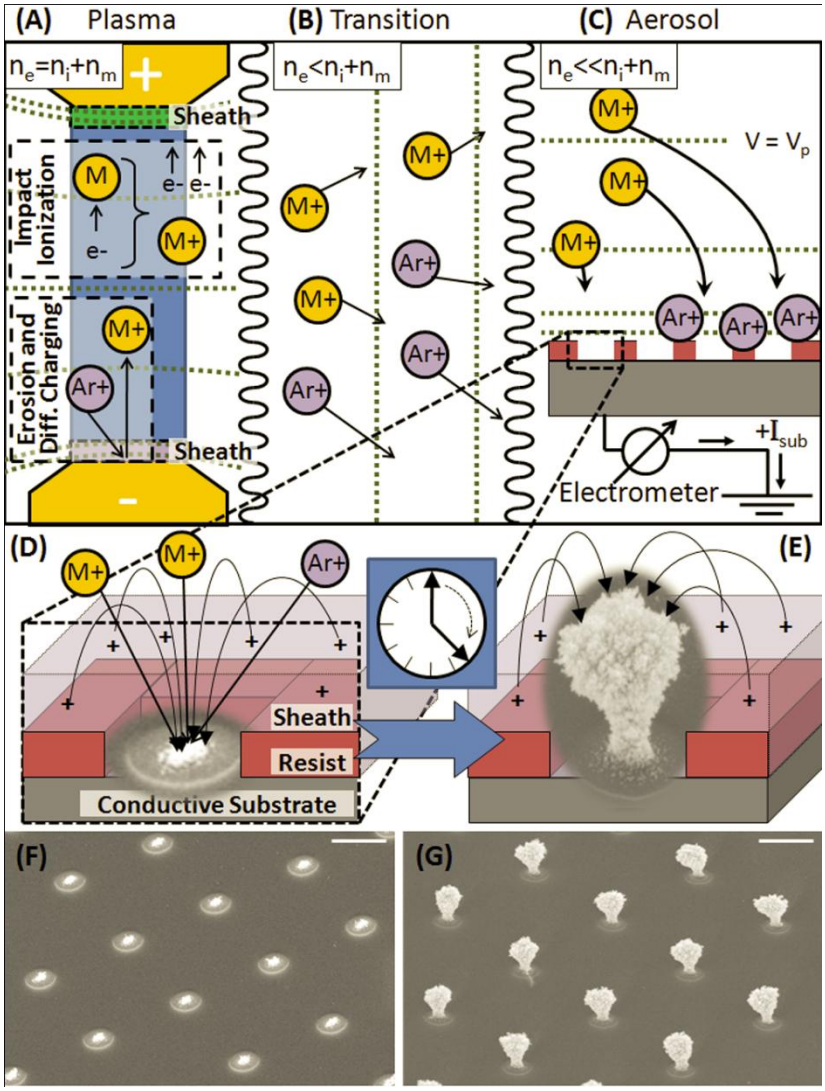

Figure 3-3. *Process details and hypothesis. (A) Nanomaterials in the arc become charged as they leave the positively charged cathode sheath (pink layer) and diffuse away through a (B) transitional region entering a cold (C) aerosol region where they are collected. (C) The collection of M+ and Ar+ ions is monitored using an electrometer that connects the sample to ground recording the steady state neutralization current. (D and E) The nanolens effect visible in the overlaid SEM results is explained using high mobility Ar+ gas ions which cause the patterned dielectric layer (purple) to float up to become positively charged (pink transparent sheath layer). The lower mobility nanoparticles (Au shown) deposit into the openings as a result of the established fringing field. Continuous nanoparticle deposition develops the pattern into tower like structures. 1 μm scale bars in (F,G).*

Figure 3-3 depicts the working hypothesis of the deposition process and provides details as to why the particles become positively charged supporting collection on grounded or negatively biased conducting surfaces. The illustration describes the case for metal electrodes (M) exposed to an argon DC arc discharge but can be extended to all the other materials and carrier gases that we investigated so far. The illustration is divided into three areas: (A) a hot plasma region with free electrons *e-*, *Ar+* ions, and positive particles *M+* of concentrations n_e, n_i, and n_m which is quasineutral ($n_e=n_i+n_m$), (B) a warm transitional region, and (C) a cold aerosol region where the positive particle/ion concentration n_i+n_m exceeds the free electron concentration n_e forming a positively charge aerosol ($n_e << n_i+n_m$). The cold aerosol region depicts a flux of positive charged particle *M+* and ions *Ar+* which is recorded using the electrometer. Visual inspection of the consumable electrodes show that the nanoparticles originate at the cathode which is eroded and consumed over time while the anode remains largely unaffected by the process. The nanoparticles diffuse through the transition region and deposit onto grounded surfaces causing discoloration visible to the bare eye within a minute. However, the nanoparticles will not coat insulating surfaces. This selectivity between conducting and insulating surfaces is illustrated in the schematic and Scanning Electron Microscope (SEM) micrographs (Figure 3-3D,E,F) where the materials deposit into 300 nm openings in a 100 nm thick insulating film of PMMA resist on top of a grounded Si chip forming tower-like structures (Figures 3-3E,G) as the deposition continues. During deposition a positive net ion current is recorded using the electrometer (Keithley, model 6517A) in the range of 0.1 nA – 20 nA where, 5 nA is a typical value. This current is related to the *M+* deposition rate. For example if we operate the system in the corona discharge regime this current drops by 2 orders of magnitudes reflected in a reduced deposition rate. The durations to develop the pattern were 2 minutes for (F) and 15 minutes for (G) both using 5 nA deposition current, yielding an average deposition rate of ~70nm/min.

We observe positive charging of nanoparticles, which is somewhat counterintuitive from a plasma physics standpoint.[67] In plasma surfaces typically acquire a negative surface charge since the electron thermal velocity

$$\sqrt{\frac{3T_e}{m}} \qquad (1)$$

exceeds the positive gas ion thermal velocity

$$\sqrt{\frac{3T_i}{M}} \tag{2}$$

in thermal equilibrium $T_e = T_i$ by roughly three orders of magnitude due to the smaller electron mass *m*. However, this negative surface charge is compensated by a sheath of positive space charge as illustrated in Figure 3-3A, pink region.[68, 69] Particles that originate at the cathode transit through this region and acquire a net positive charge (Figure 3-3A, bottom inset) through diffusion charging.[70] Electron impact ionization[71] is a second major charging mechanism which may play a role as well (Figure 3-3A, top inset). The charged particles will leave the arc vicinity crossing isopotential lines (dotted gray lines) driven by thermophoresis diffusion and convection to ultimately encounter the sample (Figure 3-3C) where they deposit on grounded or negatively biased surfaces.

Sheaths regions (purple near cathode and green near anode in Figure 5A) are confined to distances on the order of the Debye length of the high mobility electrons in the system. The anode sheath accumulates a negative space charge dominated by high mobility electrons whereas the cathode sheath is depleted of free electrons yielding a positive space charge region of primarily Ar+ considering the depicted argon plasma situation. We refer to Lichtenberg et al. for detailed calculations of the sheath region at the cathode of an arc discharge lamp. The Debye length is

$$r_D = \sqrt{\frac{k\varepsilon_0}{e^2}\frac{T_e}{n_e}} \tag{3}$$

where k is Boltzmann constant (8.62 * 10-5 eV/K) and ε_0 is permittivity of free space (8.854 * 10-12 F/m), and this electrostatic shielding length depends on the ratio between electron temperature Te and electron concentration ne. The range of possible values is great: ne = 10E16cm-3, Te = 22000K, rD = 200nm are common for a high 6A atmospheric pressure arc whereas ne = 10E8cm-3, Te = 11600K, rD = 0.7mm have been discussed for a lower current corona discharge.

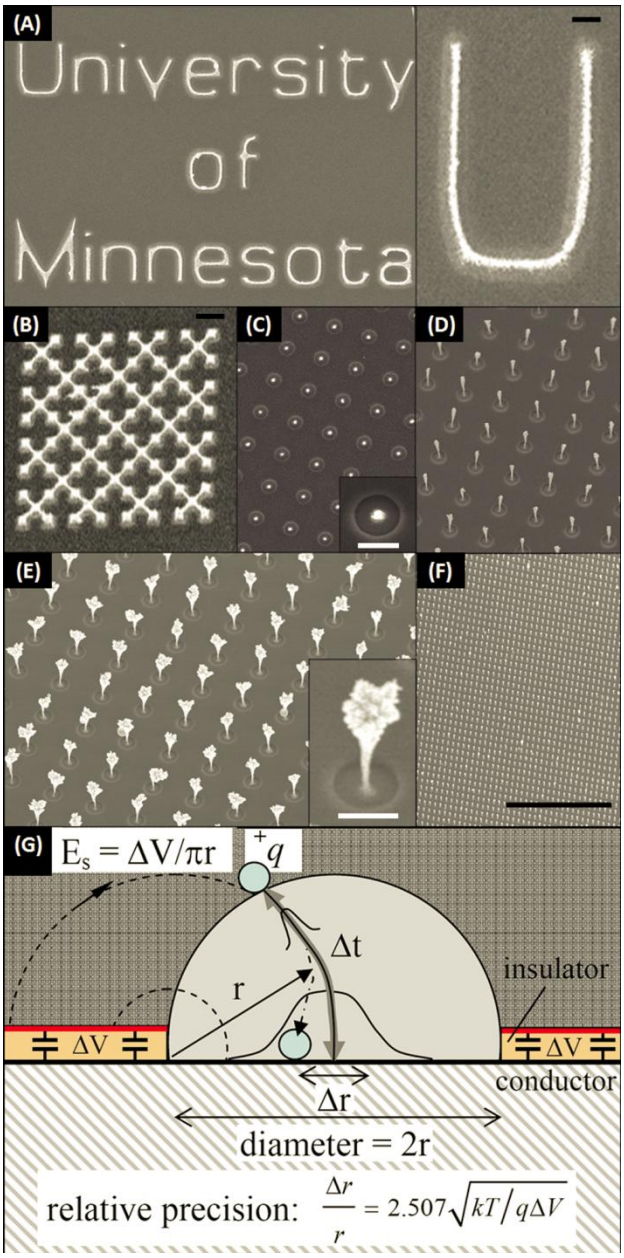

Figure 3-4. *Representative images of nanoparticle deposits limited to Au as a function of deposition time increasing from 2 minutes (A,B,C) to 15 minutes (D) to 30 minutes (E,F) at constant 10W arc discharge power. Particles deposit into openings in 80nm thin PMMA e-beam resist (A,B) or 0.5µm thick Shipley 1805 photoresist (D,E,F) with a minimal lateral resolution of 60 nm. Particles do not deposit on the resist and are initially direct to the centers of resist openings (G). Scale bars: 100nm for (A inset), 1 µm for (B), 1 µm for (C, E insets), and 100 µm for (F).*

Figure 3-4 depicts this selectivity between conducting and insulating surface showing gas-phase plating of <20 nm gold particles forming text, interconnected lines, grids, and arrays of vertical deposits on a silicon substrate that was partially shielded using a 80 nm thick e-beam patterned PMMA layers (A,B) and 500 nm thick S1805 photoresist (C,D,E,F) (details in Experimental section). The text structure (A) and interconnected grid (B) were developed in 120 seconds which illustrates that the gold particles can be deposited with 60nm lateral resolution without finding any particles on the resist itself. This is quite remarkable again showing that the insulting surfaces appear to self-equilibrate to a sufficiently high potential for the nanoparticle flux to be directed only to grounded regions. A focusing effect and a small standard deviation in the location of the deposits become apparent using 1 μm circular openings (C,D,E). Here the particles initially deposit into an area that is approximately 7 times smaller than the opening but spread out over time yielding tower like structures that can be several micrometers tall (D). This focusing effect is a function of the deposition rate and needs to be further investigated. Higher deposition rates appear to defocus the patterns. Continued deposition causes the tops of towers to broaden (E). These towers contain several hundred layers of 5-20 nm particles. Small 1 μm deposits (A,B) are uniform over large areas while tall 2μm deposits (F) begin to show some level of variations over mm sized areas.

Theory

Initial focusing of deposited nanoparticles (Figure 3-4G) has been observed previously when a surface was exposed to ions and a low concentration of nanoparticles.[20] The relative precision of focused nanoparticle deposition was found to depend on the insulator surface potential.[20] Initial deposition behavior is sufficiently similar to prior work to prompt a brief discussion of the deposition physics. Here the observed focusing effect and expected precision can be studied by solving Langevin's equations of motion of nanoparticles inside an electric field. To establish an analytical form for the relative precision, we considered a single particle at a radial distance r from the center of a patterned hole, as illustrated in Figure 3-4G. In this case, the uncertainty acquired in the particle trajectory (Δr) due to Brownian motion can be described by the root-mean-square displacement or half-width of the Gaussian bell curve

$$\Delta r = \sqrt{2\Delta t D} \tag{4}$$

where Δt is the time for a particle to deposit,

$$D = \frac{CkT}{3\pi d\eta} \tag{5}$$

is the Stokes-Einstein diffusion coefficient for nanoparticles of diameter d, viscosity η, and empirical slip correction factor C. Maximum deviation considering a Newtonian trajectory will occur at the center, where the field strength is smaller and where the time to deposit will be increased. The electric field along the central particle path,

$$E_s = \frac{\Delta V}{\pi r} \tag{6}$$

will cause the particle to follow the trajectory with a terminal velocity

$$v_t = \frac{CqE_s}{3\pi d\eta} = \frac{qE_s D}{kT} \tag{7}$$

Substituting $\Delta t = r/v_t$ yields a normalized half-width of the Gaussian bell curve in the form of Equation (1):

$$\frac{\Delta r}{r} = \sqrt{\frac{2kT}{qrE_s}} = 2.507\sqrt{\frac{kT}{q\Delta V}} \tag{8}$$

Equation (8) provides a number of important insights into electric-field-directed self-assembly processes. First, the key measure of the expected focusing will be the potential difference between charged and uncharged areas. Values of $q\Delta V$ larger than kT are desired. Second, the relative precision is independent of the size of the pattern and therefore scaleable. Third, the precision can be increased by increasing the particle charge.

Following initial focused depositon the process is allowed to continue until deposited conductive nanoparticles eventually alter the electric field lines. The towers grow with electric field lines pointing towards the tops of the nanoparticle towers which exceed the height of the confining charged resist. Due to this increased distance between depositing nanoparticle and charged resist, nanoparticle mass transport becomes more poorly

focused to the center of the resist openings resulting in mushroom-shaped nanomaterial towers.

Figure 3-5 shows a process and results of programmable deposition of three different materials Au, ZnO, and Ge using sequentially biased electrodes, and the concept of programmable deposition is applied to produce a multimaterial sensor array with humidity and photosensitive regions. The illustrations (A, B and C) depict the concept. First gold nanoparticles are plated on a grounded organic conductor P3HT (poly 3-hexylthiophene) while nearby P3HT lines and glass surfaces (preparation details in Experimental section) electrically float up to a sufficiently high electrical potential preventing gold nanoparticle deposition in the surrounding area. Resistance measured for the initial P3HT line exceeded 10MΩ. Covering the P3HT line with Au nanoparticles reduced the resistance to 2.9kΩ. The Au line was 3 mm long, ~500 nm wide, and plated be 1 µm thick. Applying Ohms Law yields a measured resistivity of $4.8*10^{-5}$ Ω-cm which is close to $2.26*10^{-6}$ Ω-cm (accepted value for Au at 298K). After the Au line deposition the arc electrodes were replaced to deposit ZnO onto a separate originally floating P3HT line which is now grounded while everything else is left floating (Figure 3-5B). ZnO nanoparticles now deposit selectively onto the grounded electrodes as before in the case of Au. The ZnO example illustrates what happens after 30 minutes of deposition. The films begin to overgrow the grounded region forming roughly a hemi-cylindrical structure.

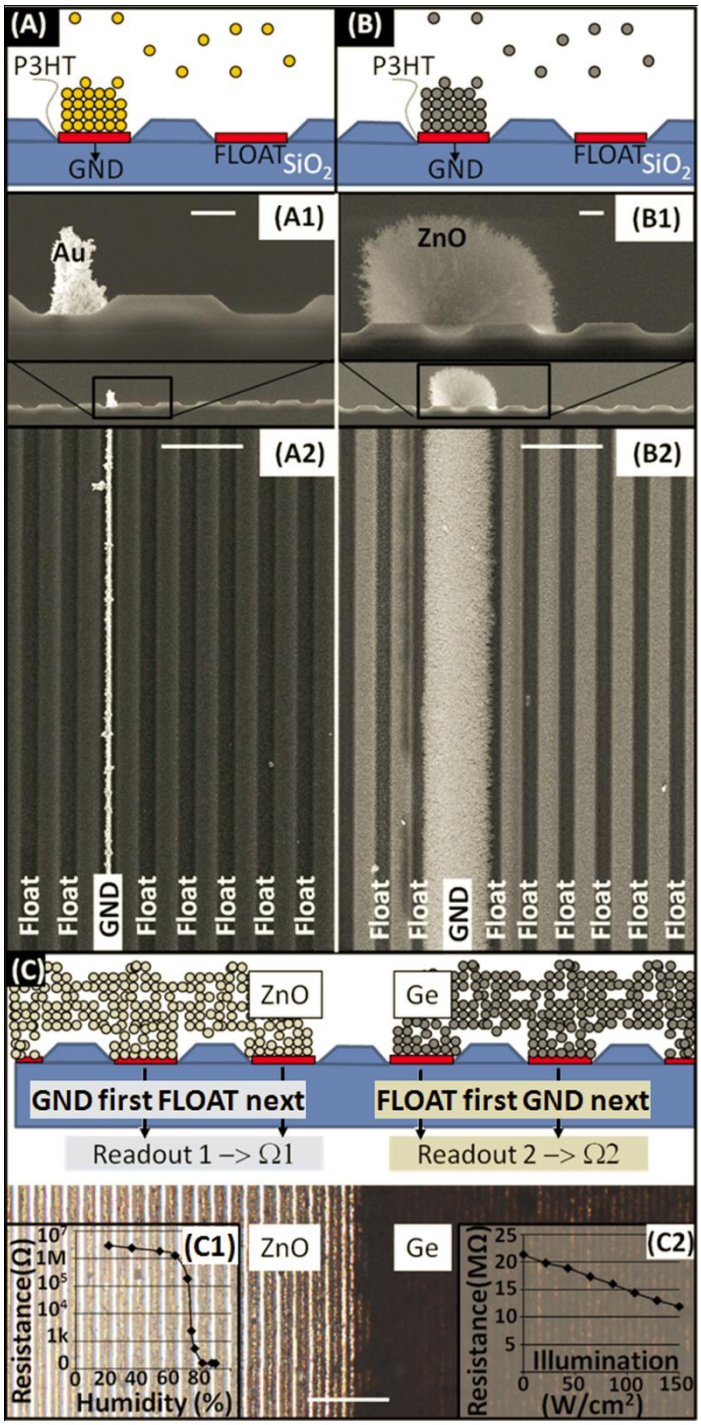

Figure 3-5. *Concept and results of programmable multi-material (Au, ZnO, Ge) deposition forming (A) conducting and (B) semiconducting traces, or (C1) humidity and (C2) light sensitive areas. (A,B) Grounded 1 µm wide P3HT lines attract nanoparticles forming a continuous interconnected structure as illustrated in the cross-sectional (A1,B1) and top-down (A2, B2) SEM images. Au particles pack into denser structures*

than ZnO and yield smaller line widths for identical deposition time (30min) and arc power (10W). (C) Programmable deposition procedure using sequentially grounded electrodes applied to form sensing layers where the same electrodes are subsequently used for readout. During the first deposition cycle all the electrodes on the left side are connected to ground until ZnO forms a merged film on the left side. This is reversed in the second cycle to the right until Ge covers the right side of the chip which is visible in the darker appearance of Ge under an optical microscope. The two film regions bridge the electrodes underneath and yield a characteristic resistance which reduces with humidity for ZnO (C1) and illumination for Ge (C2). 1µm scale bars in (A1,B1), 10µm scale bars in (A2,B2), and 20 µm scale bar in (C).

This concept of programmable deposition and overgrowth bridging nearby electrodes can be used to program the deposition of multimaterial sensor arrays while providing a parallel readout on a single chip. The concept is illustrated for ZnO and Ge in Figure 3-5C which results in a continuous interconnected film of ZnO on the left and Ge on the right. The films bridge adjacent conductive lines (preparation details in Experimental section) whereby the bridge resistance varies with exposure to light (Ge) and humidity (ZnO). The magnitude of the resistance change in Ge due to illumination is attributed to long minority carrier lifetimes in the crystalline Ge. The large increase in the conductivity for ZnO is likely directly related to the high porosity and large surface area which is apparent in the cross-sectional SEM image (3-5B1) discussed before.

To understand why a uniform deposition is observed and what the potential limitations might be the thickness of the space charge sheaths surrounding the sample surface has to be considered. These sheaths were depicted in Fig. 3-3D and are analogous to the double layers surrounding the surfaces in the liquid phase and thicknesses are on the order of the Debye length.[71] Adjacent areas on the sample within the distances of the characteristic Debye length will compete to attract nanoparticles which arrive at this boundary layer primarily driven by diffusion.[72] As in the liquid phase the Debye radius r_D is inversely proportional to the square root of the average number concentration n_0 of charged particles above the sample surface and is given for the gas phase by Equation (9).

$$r_D = \sqrt{\frac{1}{n_o}}\sqrt{\frac{k\varepsilon_0}{e^2(1/T_e + 1/T_i)}} \tag{9}$$

For Equation (2), k is the Boltzmann constant, ε_0 is the free space permittivity, and e is the elementary charge. T_e and T_i are the electron and ion temperatures which are assumed to be at room temperature in the aerosol regime. The number concentration n_0 of charged particles that can be supported was estimated using conductivity measurements as described in the supplementary information controlling the distance to the arc and the arc current. Typical values ranged between $10^9 cm^{-3}$ to $10^7 cm^{-3}$ corresponding to a Debye length in the range of 50-500μm, respectively. These n_0 values are close to previously published values of ($10^9 cm^{-3}$) recorded near charging sources in atmospheric pressure aerosol.[73] The numbers are in contrast to the situation in standard vacuum deposition systems where the Debye length easily exceeds the dimensions of the deposition system by orders of magnitudes since the number concentration of gas molecules drops proportionally with pressure. At the same time the Debye length remains orders of magnitudes larger than the sub micrometer values found in liquid phase. Despite this important difference it has become small enough to enable in-situ selected area deposition. While adjacent areas on the sample compete for nanoparticles within the Debye radius the formation of arbitrary patterns (Figure 3-4) can still be achieved. The implication of a sufficiently small Debye length attained at high pressure is that the electrostatic deposition behavior becomes decoupled from the source. Less stringent requirements for symmetric designs with respect to the particle source are a direct result.

Figure 3-6 investigates the presence of stray particles testing the deposition on isolated lines and interdigitated electrode structures. The dimensions of the patterns are scaled to provide a larger field of view showing 15 μm (A) and 80 μm (B) pitched patterns. Nanoparticle deposition selectivity is high: even after extended deposition times these test structures did not produce an observable amount of stray particles onto the insulating surfaces or floating metal lines. The correctly deposited Au was 3μm tall which represents at least 100 particle layers. We expect the selectivity of sequential deposition steps with multiple material types to be nearly as high as the selectivity of a single step since crosstalk between lines appears to be minimal.

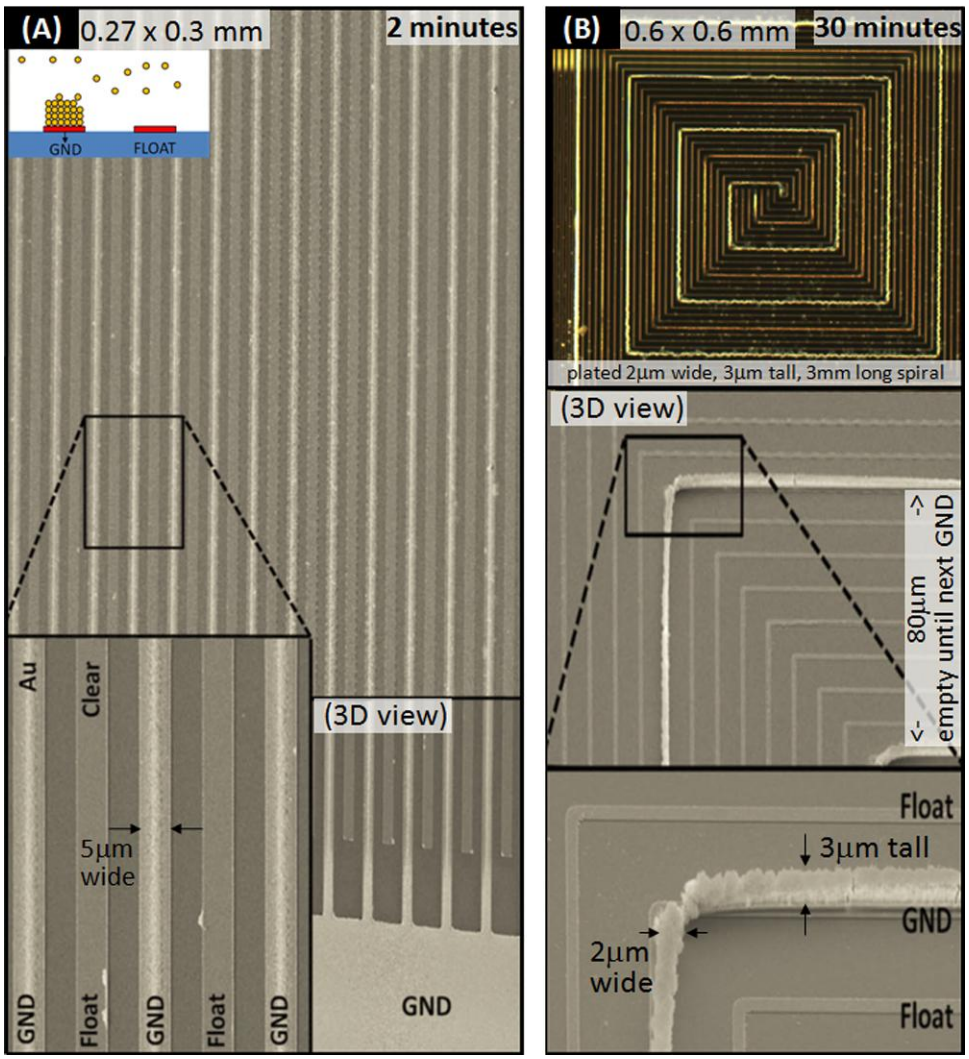

Figure 3-6. *Schematic and results of programmable selected area gas-phase electrodeposition after 2 min (A) and 30 min (B) deposition. The pad region in (A, bottom inset) shows the level of uniformity transitioning from a large (150x150 µm^2) single domain to spatially separated 5µm wide lines. Deposition occurs only on grounded areas; floating conductors and insulating surfaces remain empty. Increasing the size of the empty regions from 15 µm (A) to 80 µm (B) maintains this selectivity. The optical microscope image (B) depicts a spiral interspaced with 7 empty ones that were left floating yielding a single 2 µm wide, 3 µm tall, and 3 mm long Au line.*

3.3 Conclusion

Comparable to liquid phase electrodeposition, the reported gas phase analogue can deposit material into addressable areas forming vias, interconnects, or patterned multimaterial films in a programmable fashion. The process was tested using a limited set of technologically relevant functional materials including Au, Si, Ge, TiO_2, and ZnO at sizes of 20nm and below as confirmed by TEM, SAED, EDX, and XRD. We anticipate that the process can be extended to other materials and gas phase systems with some alterations. The uniformity on a macroscale is presently limited by diffusion since we use a single point source fixed in space. Scaling to larger sample areas would require the use of either multiple sources or translational motion analogous to what has been used in other gas phase deposition systems. The ability to maintain uniformity when developing arbitrary patterns on a nanoscale requires a sufficiently small Debye length which in turn favors higher pressure aerosols to provide a high concentration of charged particles/ions and deposition rate. The estimated values are sufficient to support selected area programmable deposition of a variety of different patterns including text, connected and disconnected structures. Operating a system at atmospheric pressure has the advantage of simplicity since neither vacuum pumps nor high pressure enclosures are required. Pressurized systems, however, would likely further increase the area selective deposition rate beyond the current 100 nm/min value. The current area selective rate is in between the 10 nm/min rate of non-selective vacuum deposition systems and typical 1 μm/min rate of area-selective electroplating methods. Variations in the film thickness, extension to large area deposition using multiple spatially separated discharge regions, passivation of surface and interface states are important aspects that will require further research and new and improved designs.

A potential future application of the gas phase electrodeposition technique can be found in the field of printable electronics. It contrasts the use of solution processable electronic inks and inkjet type printing concepts to deposit nanomaterials. Current inkjet based deposition systems have low resolution and throughput. The inks require surface functionalization to stabilize the particles which often interferes with the desired electronic properties. Alternatively the discussed *in-situ* gas phase synthesis and deposition system offers a more parallel route to the formation, deposition and integration

of higher performance materials than liquid phase concepts. High temperature processes can be used to produce the materials that can then be deposited onto low temperature substrates eliminating any extra processing steps or a transition into the liquid phase. As such the present technique is highly parallel and does not require the use and alignment of scanning nozzles or the formulation of stable liquid particle suspensions. These advantages come at the cost of needing pre-patterned substrates to direct the deposition.

Chapter IV

Gas Phase Electrodeposition: A Programmable Multimaterial Deposition Method for Combinatorial Nanostructured Device Discovery

En-Chiang Lin, Jesse J. Cole, and Heiko O. Jacobs

Reproduced with permission from:
Nano Letters 10, 4494-4500 (2010)

4.1 Introduction

Inorganic nanomaterials in the form of nanoparticles and nanowires have attracted attention due to their unusual properties including quantum size effects, high surface area-to-volume ratio, and increased catalytic activity. These properties have influenced almost any research discipline in recent years including the fields of printable electronics, optoelectronics, physical sensors, solar cells, biological screening, and environmental protection[1-5]. Today there is a host of synthesis techniques available to form the desired inorganic nanomaterials which can be grouped into two classes: low temperature wet chemical and high temperature gas/vapor phase methods. Gas/vapor phase methods such as thermal flow synthesis[6-8], laser ablation[9], sputtering[10], plasma induced synthesis[11], and arc discharge[12, 13] can produce nanoparticles and nanowires of various types including high temperature and high performance semiconductors that are difficult to make using low temperature wet chemical methods.

A challenge today can be found in the design of gas phase systems that combine high temperature synthesis with low temperature local area deposition on foreign substrates for printable electronics applications. Selected area deposition schemes are well established in the liquid phase but remain largely absent in the gas phase. Current direct write gas-phase deposition methods use nozzles, or aerodynamic beams[14, 15] to deposit the materials locally in a serial fashion with 30 μm resolution. Selected area deposition has also been reported using pre-patterned surfaces. For example, it has been demonstrated that charge patterned insulators can be used to attract a limited amount of oppositely charged particles[16, 17] with <100 nm resolution. While pre-patterned surfaces provided much higher resolution they remained limited to 2 dimensional deposits of a few monolayer thicknesses. The use of pre-patterned surfaces had the additional disadvantage that materials could not be altered to vary across the substrate. Very high resolution but mono-material and two dimensional prints have been the state of the art using pre-patterned surfaces.

Recently Cole *et. al.*[21] reported a deposition system which eliminated the limitations that the deposits can only be a few monolayers thick by introducing a concept that

provides localized charge dissipation. This report extends this printing concept to a multi material deposition scheme demonstrating three dimensional nanostructured deposits which are applied in the combinatory discovery of nanostructured devices. Specifically, we report a multi-material selected area deposition process that produces <5 nm nanoparticles of Pt, Ag and W which are subsequently deposited into photoresist openings with sub 100 nm lateral resolutions and aspect ratios of 10. We demonstrate multimaterial nanostructures that contain sections of Pt, Ag and W, whereas individual thickness, density, and height is varied and the sequence of the material is switched and selected to be different from one domain to the next. The reported gas phase process shares some of the characteristics of electrodeposition in the liquid phase. The process allows us to control the flux of charged material to locations with 100 nm lateral resolution to form bridges and interconnects in selected domains or, in the simplest case, to form straight metallic nanowire arrays whose height and density are adjusted to vary across the substrate.

This reported process can be applied to the combinatorial screening of various types of nanostructured deposits for electronic and optoelectronic device applications/discovery. As a first demonstration in this direction we test whether the tool can be used to identify/discover electrode designs that improve the carrier extraction efficiencies of bulk heterojunction photovoltaic cells. The approach discussed here does not use mechanical shutters to turn ON/OFF deposition in certain areas and provides programmability with much higher resolution and feature density than prior concepts that have been applied to field of optoelectronics and photovoltaics[24-27]. We explored different interpenetrating electrode designs in particular 3D nanowire-based electrode arrays where height and density is adjusted from one domain to the next. The protocol varied pitch from 3 μm to 5 μm and height from 500 nm to 900 nm to explore the impact on absorption efficiency (η_A) and minority carrier extraction efficiency (η_{ED}). The completed solar cell domains share the same substrate, processing, and testing conditions. Short circuit current densities ranged from 7.7 to 12.2 mA/cm^2. The relative power conversion efficiencies (PCE) increased by 47% in domains that carried dense nanowire arrays when compared to the flat reference on the same substrate.

4.2 Results and Discussion

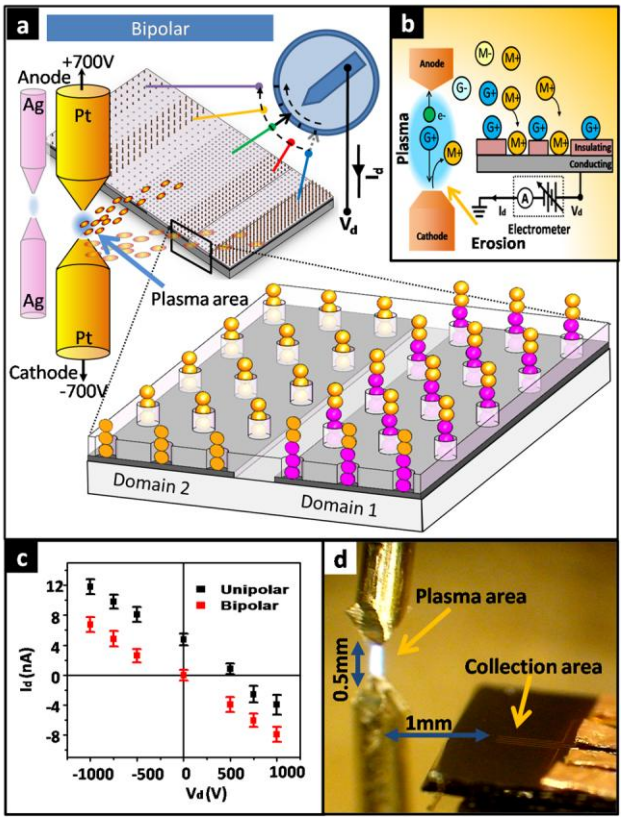

Figure 4-1. *Programmable Multimaterial Deposition Process. (a) Schematic depicting a plasma region with two sets of consumable Ag and Pt electrodes next to a substrate that collects charged nanomaterials using externally-biased electrodes to control the material flux and to turn deposition ON/OFF in selected domains. The domains carry a patterned photoresist which act as deposition guides that funnel the material into the openings. (b) Basic concept depicting that charged nanomaterials are produced by cathode erosion and ionization inside the plasma region whereby material flux is diverted towards the biased substrate domains leading to a measurable domain current I_d; I_d reflects the rate of charge deposition and dissipation on a selected domain. (c) Relationship between the current I_d and domain voltage V_d for bipolar (+700, -700V) and unipolar (+1,400V, 0V) biased arc discharge electrodes (discussed in text). (d) Photograph with physical dimension.*

Figure 4-1 describes the programmable gas phase nanomaterial electrodeposition system where charged material is extracted from the hot plasma region using an externally-biased sample that is located in the surrounding low temperature aerosol region. The system is similar to the original implementation[21] with the exception that it contains multiple metal electrodes Pt, Ag and W (1mm rod diameter, Sigma-Aldrich) of the source material instead of a single semiconducting electrode source. The process uses a conventional <100W DC arc discharge where a concentrated plasma surrounds the tip of the consumable cathode. The sample is located in the surrounding aerosol region and carries differently-biased domains to attract charged material of a desired polarity. Furthermore, domains are partially screened using a patterned thin layer of Microposit S1805 photoresist which provides pores and openings to the underlying conducting and externally-biased domains. The resist prevents charge dissipation and the material seeks to deposit into the openings. In the illustration domain 1 is activated first for a certain deposition time of silver (pink color) and a slightly smaller amount of time in the deposition cycle of platinum (orange color) leading to the respective film thicknesses. Domain 2 is turned ON in the third deposition cycle to receive a platinum layer (orange) as the first layer. No shutters are involved.

Figure 4-1b depicts the current understanding of the process of *(i)* particle generation, *(ii)* charging, and *(iii)* selected area deposition. *(i)* The process of particle formation through cathode erosion using atmospheric pressure arc discharge is well established[74-76]. Electrons generated in the plasma region are accelerated by the applied electric field to the anode, producing gas ions (G+) through impact ionization. The gas ions (G+) move and impact the cathode which leads to cathode erosion. *(ii)* The eroded material (M) leaves the cathode that is surrounded by a positive (G+) space charge region and picks up positive charge resulting in the depicted (M+) particle; negative and neutral particles will be present as well. *(iii)* Selected area deposition is possible since all charged species are influenced by nearby electrodes. Depicted is the case for a negatively-biased (V_{sub}<0) domain (Fig. 1b). The deposition process should be considered as an electrodynamic process since the field distribution evolves over time. Mass and electrical mobility of the involved species is important. The depicted gas ions (G+) have a higher electrical mobility than the heavier metal particle. On a time scale and in the initial stages of the

experiments the gas ions (G+) arrive at the sample surface first, which results in the depicted sheath of space charge (G+) on the sample surface and alters the potential distribution. Under equilibrium conditions a flux of positive material is established which flows to the conducting and bare electrode sites. The resulting electrical domain current, I_d is recorded with an electrometer (Keithley, model 6517A).

Figure 4-1c depicts a graph of the recorded domain current I_d as a function of the domain voltage V_d which is applied by the electrometer to remove the charged species from the gaseous environment. The graph depicts the results of the ionic currents and particle flux for two different types of discharges: (i) bipolar (+700V upper electrode, -700V lower electrode) and (ii) unipolar (+1,400V, 0V). We choose to use the bipolar case as it provides better control to turn ON and OFF deposition in certain areas than the unipolar scheme that we used initially. The bipolar discharge has the advantage that grounded substrate domains V_d= 0V yield zero deposition current which is not the case for the unipolar scheme where a positive domain voltage is required to block deposition.

The dimension of the implementation is shown in the photograph (Fig. 1d). The electrodes are enclosed inside an 8,000 cm^3 plastic polypropylene chamber that allows the control of the pressure and gaseous environment. The reported results here focused on Pt, Ag and W, which were found not to be as prone to oxidation as previous experiments that worked with Si and Ge where specialty gases had to be used. Instead all deposition experiments were performed under a relaxed air environment (78% N_2 and 21% O_2) at atmospheric pressure.

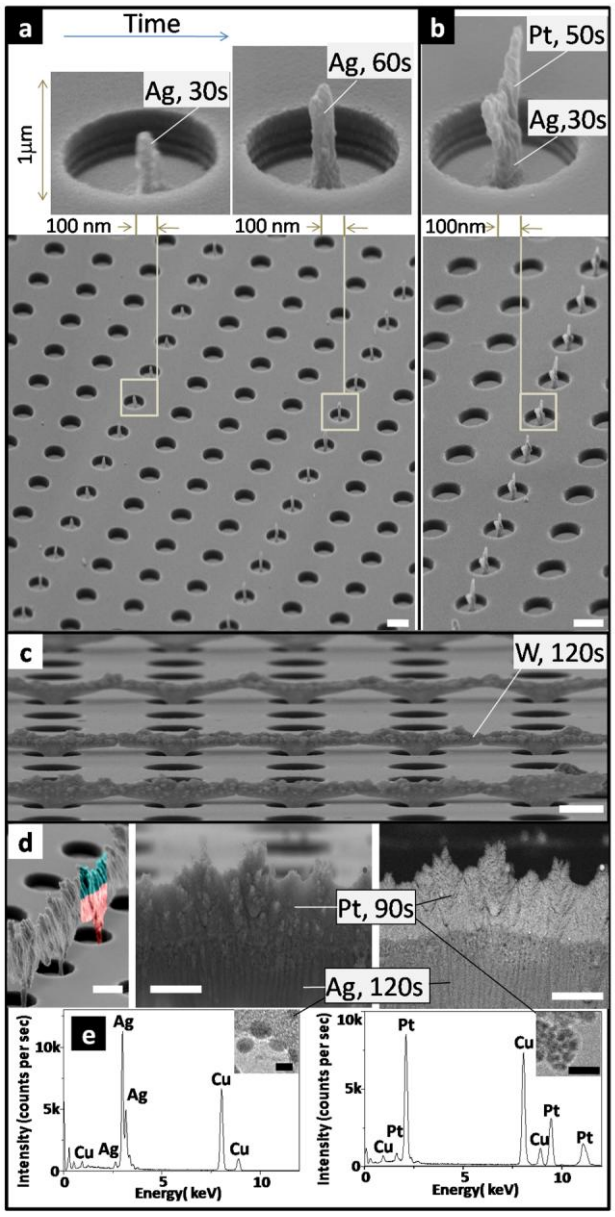

Figure 4-2. *Results of multi-height (500 nm, 1 µm, 2 µm) and multi-material (Ag, Pt, and W) towers and bridge arrays. (a) Lines of Ag deposits on doubling the height from one line (30s) to the next (60s) with three empty domains in between. Domain pitch is 3 µm. Nanolens effect is visible where the material is funneled into the center of the 1 µm wide opening. (b) 30s Ag followed by 50s Pt depicting the onset of forking to nearest neighbors. (c) 120s W bridging to nearest (3 µm pitch) neighbor instead of farthest (9 µm pitch) neighbor. (d) Bilayer bridges containing Pt and Ag as confirmed by EDX with a primary particle size that is typically smaller than <5 nm of Ag and <2 nm for Pt as*

confirmed by TEM. The interface is visible in the backscattered electron microscope image to the right. 1 μm scale bars in (a)-(d), 5 nm scale bars in the TEM inserts.

Figure 4-2 depicts results of localized deposition of various amounts (500 nm – 2 μm) of Ag, Pt, and W where material type, height, and structure is adjusted from one domain to the next. Figure 4-2a depicts different amounts of silver that have been deposited onto selected domains in a two-step sequence. Selection is done by applying -150 V to 1 μm wide conductive copper domains that run underneath the visible 1 μm diameter and 3 μm pitched photoresist (Microposit S1805) hole pattern. The deposition times on the left and right were 30s and 60s, respectively. The heights were approximately 550 nm and 1100 nm yielding a deposition rate of 18 nm/s. This rate is a factor of 20-200 higher than what is achieved in conventional vacuum thermal or e-beam evaporation systems where 0.1-1 nm/s is typical. For 1 μm diameter openings, incoming material is funneled into a region that is approximately 10 times smaller than the opening itself with a positional accuracy of 20-30nm (STD). The positional accuracy is a relative alignment accuracy with respect to the given photoresist structure; absolute alignment accuracy remains limited by the mask aligner. Resulting deposits grow into well-defined needles/towers with a diameter of about 100 nm. The insulating surface cannot dissipate charge and prevents the deposition of material, which is visible in the figures; no particles are found on the photoresist itself. In fact, the incoming positive material maintains a distance away from the photoresist, which requires a potential landscape or potential trough that favors the material to follow down a 100 nm thin channel to the center of the photoresist opening in the illustrated case. This means that the insulator floats up to a more positive potential in the initial stage of the experiments which is maintained under equilibrium conditions and is utilized here to form nanolense arrays. Incoming material deposits on top of the advancing structures and maintains the cylindrical nanolense symmetry well above the surface of the 500 nm deep resist openings before they begin to spread out and change shape. Structures maintain the shape if the deposition process is stopped before they grow much taller than the photoresist film thickness itself; much taller structures will change shape similar to the “mushrooming” effect in electrodeposition in the liquid phase which is shown in the supplementary Figure 4-S1.

While it is more difficult to predict the shape under prolonged deposition the structures remain well defined. This is illustrated in Figure 4-2b where we have selected the deposition of two different materials. The structures contain about 500 nm of Ag and 800 nm of Pt and show the onset of forking to nearest neighbors. Forking to nearest neighbors is due to the collective behavior of the underlying electrode, photoresist pattern and emerging nanostructures. Both far and near fields need to be considered to understand the forking behavior. At a distance that is sufficiently large the underlying negatively-biased holes are seen as a negative line, which concentrates incoming material into a 2-dimensional sheath that is directed towards the surface. In close proximity the 2-D sheath separates into isolated flux channels until they reach the surface of the emerging nanostructures.

The separation into isolated flux channels leads to the observed forking and ultimately the formation of interconnects between nearest neighbors. This is illustrated in Figure 4-2c where the concept is used to form interconnects between nearest neighbors using a third material, tungsten, and 120s deposition. Figure 4-2d repeats this experiment forming a stack of two different materials, 120s of silver and 90s of platinum. These are tilted views of the sample. The green and pink colors were added to help distinguish the different domains. The interface is well resolved in the backscattered electron image (BSE), which is sensitive to the atomic number difference of the materials; those with higher atomic numbers (Pt in the shown case) appear brighter. Figure 4-2e contains material-specific data of the materials that are formed using the arc discharge process. Specifically, we collected some of the material on a copper transmission electron microscope (TEM) grid and analyzed the samples in a TEM (Phillips FEI T12). The inserted TEM image depicts 5nm silver and 2nm platinum particles. The particles are typically smaller than 5 nm and are confirmed to be Ag and Pt using Energy Dispersive X-ray Spectroscopy (EDS). The TEM image and EDS for tungsten are included in the supplementary section.

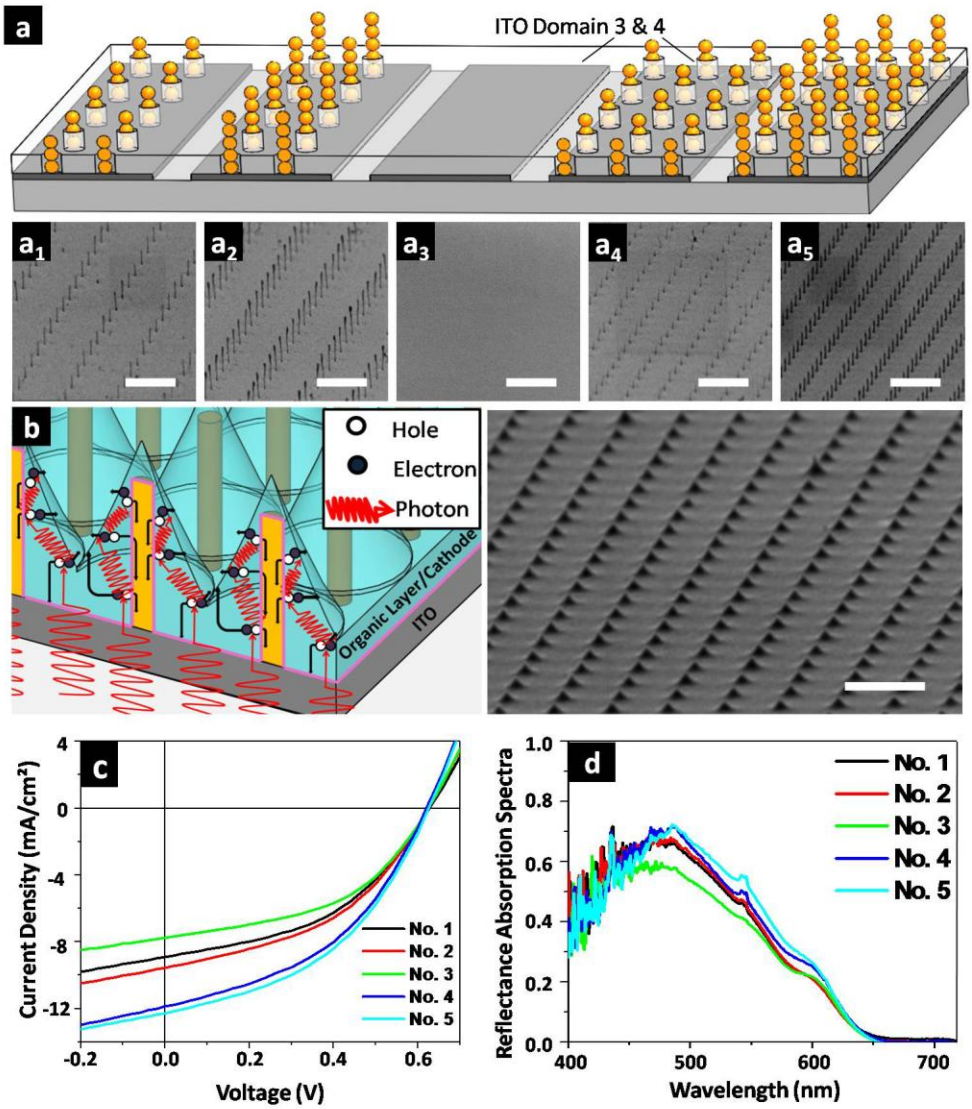

Figure 4-3. *Combinatorial screening of nanostructured Pt nanowire electrodes adjusting pitch and height impacting carrier extraction and absorption efficiencies in organic P3HT: PCBM bulk heterojunction photovoltaic cells. (a) Schematic using photoresist guides to define circular opening using 5 different domains to receive 600, 900, 0, 500 and 800 nm of Pt; the pitch is 5 µm on the left (a1), (a2) and 3 µm (a3), (a4) on the right; (b) Graphical representation of the completed structures depicting nanowire anodes that penetrate the organic layer next to the SEM image of the P3HT: PCBM bulk heterojunction photovoltaic cell on domain 4; scattering is depicted to take place at the embedded Pt nanowires and the conical Al coated top surface. (c), (d) I/V curves and*

reflectance absorption spectra of the different domains. 5 μm scale bars in (a1)-(a5) and the inset of (b).

Figure 4-3 provides results where the programmable gas phase deposition tool has been applied to the general idea of combinatorial screening of nanostructured deposits for electronic and optoelectronic device applications. The specific demonstration focuses on the identification of nanostructured electrode designs that improve the carrier extraction efficiencies of bulk heterojunction photovoltaic cells. The p-n junction where electron-hole pairs are separated is no longer planar in these devices and the electrical contacts and geometry is one of the most critical elements. The use of nanostructured 3D electrodes has been reported previously to improve device efficiency[77]. However, little is known how the density and height variations impact the device performance. The current practice of processing separate substrates in different runs often yields inconclusive answers. To overcome this challenge of processing different substrates we deposited domains of nanowire arrays with different heights and density on a single substrate by controlling the bias levels in the different domains. The protocol varied nanowire pitch from 3 μm to 5 μm and height from 500 nm to 900 nm from one domain to the next. Short circuit current densities (J_{sc}) ranged from 7.7 to 12.2 mA/cm^2. The power conversion efficiencies (PCE) increased by 47% in domains that carried dense nanowire arrays when compared to the flat reference topology on the same substrate.

Figure 4-3a illustrates the procedure and the results whereby the substrate was divided into 5 separate domains. Individual domains were formed using 500 μm wide and 2 cm long and 150 nm thick ITO regions that are located underneath a 500 nm thick Microposit S1805 photoresist. The resist was patterned to provide 1 μm diameter openings to the ITO domains. The pitch was 5 μm on the left (domains 1&2) and 3 μm on the right (domains 4&5). Domain 3 served as a reference and was not patterned. We first connected domain 1 to the negative bias and grounded the other four ITO domains to prevent deposition in undesired areas. We followed the same procedure on domains 2-5. The deposition times were 40s, 60s, 0s, 40s, and 60s; deposition material was platinum in each case. The SEMs (a_1-a_5) depict the resulting 80-150 nm diameter deposits whereby the height varied from left to right. Specific height values were 600, 900, 0, 500 and 800 nm. The histogram in supplementary Figure 4-S3 depicts the measured variation in height

in domain 5. The standard deviation (STD) was less than 13.1 nm for the 800 nm tall structures. The supplementary Figure 4-S4 provides a larger area picture to illustrate the uniformity.

It shows the processing steps and the respective SEMs that are required to complete the devices in supplementary Figure 4-S5. The steps are: 1. nanowire deposition using photoresist guides and bias control, 2. removal of the photoresist guides using an oxygen plasma, 3. spin coating of the electron blocking layer (PEDOT: PSS), active blend layer (P3HT: PCBM), and 4. vapor deposition of lithium fluoride (LiF) tunneling layer and aluminum top contact. The graphical representation in Figure 4-3b shows the 3 dimensional cells and its basic operation. The film thickness and energy level diagram of the used materials are included in the supplementary Figure 4-S5. The structure is illuminated from the bottom and electron hole pairs are produced in the active blend layer and separated by the built-in potential between the HOMO of the P3HT donor and the LUMO of the PCBM acceptor material[78]. Holes are collected by the Pt nanostructures and the ITO substrate while electrons are collected at the LiF/Al conical contacts. The graphical representation illustrates wide angle photon scattering due to the curvature of the top LiF/Al reflective contact and bottom nanowire contact where scattering takes place. Wide angle scattering and light trapping is used in the following section to explain the observed measurement results.

Table 4-1. Device performance in the respective domains

Domain	V_{oc} [V]	J_{sc} [mA/cm^2]	FF [%]	PCE [%]	Relative PCE changes [%]
No. 1	0.631	8.92	43.9	2.47	9.29
No. 2	0.627	9.57	43.4	2.61	15.4
No. 3	0.623	7.76	46.8	2.26	0
No. 4	0.621	11.88	43.1	3.18	40.7
No. 5	0.626	12.28	43.4	3.34	47.7

Figure 4-3c depicts the recorded current-voltage characteristics. The calculated device parameters are summarized in Table 1. The tabulated fill factor FF represents the ratio between the measured maximum output power normalized by the product of recorded open circuit voltage V_{oc} and recorded short circuit current I_{sc}. The active area of each domain was 0.02 cm^2 which was determined using the dimensions of the intersecting 500 μm wide ITO bottom and 4 mm wide aluminum top contact. Domains with Pt tower deposits performed better than the flat reference domain No.3. The relative power conversion efficiency was enhanced by 9.29%, 15.4%, 40.7% and 47.7% for domains 1, 2, 4 and 5, respectively, when compared to the flat reference domain 3. Most notably, the nanowire deposits have a strong effect on the recorded short circuit current and almost no effect on the open circuit voltage. Dense arrays in domain 4 and 5 produced higher currents (11.9-12.3 mA/cm^2) than the less dense arrays in domain 1 and 2 (8.9-9.6 mA/cm^2) or the flat reference (7.8 mA/cm^2). Increasing the height of the towers from 500 nm to 900 nm improved the devices as well but at a lesser rate than doubling the density. We also tested wires that were >1.5 μm long and found these to work less favorable; this was attributed to the onset of shorts since some of the wires had an insufficiently thin coating at their top. Five experiments on separate substrates all found domain 5 to have the highest performance. Figure 4-3d shows the optical absorption spectra, which suggest that the improvement of the device is at least in part due to an increased absorption. The spectra were collected from each domain using a reflection fiber optic micro spectrometer (Ocean Optics, USB4000 VIS-NIR) with a spot size of 400 μm. For example, at 485 nm the relative absorption increased by 15%, 17%, 25% and 26% for domains 1, 2, 4 and 5 when compared to the flat reference. The absorption spectra of the domains with nanostructures are also slightly broader than without. These results are in agreement with an earlier study where nanostructured topologies increased light trapping and adsorption[79, 80]. The increased optical absorption alone (up to 26%), however, is insufficient to explain the relative increase in efficiency (up to 48%) for the dense nanowire arrays when compared with the flat reference domain. This mismatch can be explained by the fact that penetrating 3D electrodes are also known to improve electron-hole pairs separation and collection[81]. Like conventional nanowire-based architectures

our 3D nanostructured electrodes shares this general idea and should provide a greater degree of freedom for the collection of holes at the Pt towers and electrons at the Al top contact. The combination of the two mechanisms -- enhancement of light absorption and improvement of carrier collection -- is likely the cause for improvement of the short circuit currents in the different domains. Despite the improvements, the reported power conversion efficiencies remain lower than the current record [82-84]. Our devices are not fabricated under the exclusion of oxygen which is known to limit the efficiency to the reported values. For example, domain 5 short circuit current drops by 58% after 10 hours of air exposure, which is a common problem for organic thin film solar cells. The exposure to air is presently limited to 10 min but is not completely eliminated since the characterization and evaporation tool are in physically different locations. The strength of the combinatorial approach however remains. It provides many different domains and a flat reference on a single substrate, which provides a more reliable comparison since all domains are exposed to the same testing and environmental conditions.

4.3 Conclusion

In conclusion, the developed process can be used to form charged, <5 nm sized particles (silver, tungsten, and platinum) at atmospheric pressure. The material can be deposited to form thick 500 nm - 2 µm nanostructured deposits on selected domains. The sequence and amount of material can be mixed and matched yielding multi-material deposits like bridges, towers, interconnects, and nanowires where height, density, and material composition can be adjusted from one domain to the next. We anticipate that the process can be extended to other metals as well as semiconductors. Here we used an oxygen-containing environment to deposit metallic material that did not oxidize readily. To extend the atmospheric pressure process to fabricate non-oxidized semiconducting nanostructured deposits is likely going to require a transition to an oxygen-free environment. Little is known about atmospheric pressure deposition systems, which appear to have many distinguishing features when compared to vacuum vapor phase deposition systems. This study reveals that the deposition rate can be at least a factor of 10 higher. The material can be deposited onto desired locations with a minimal lateral resolution of 50-100 nm and a positional accuracy of 20-30nm (STD). No liftoff is

required and less material is lost as a result. The overall cost to build this system is less than $1,000 since it operates at atmospheric pressure. The point source used, however, has some limitation with respect to uniformity if one considers larger (>1 cm^2) samples. This could be overcome by extending the process to tip arrays or orbiting substrates which has not yet been tested. Instead, we decided to apply the method to identify, in a combinatorial way, 3D nanostructured electrode designs that improve light scattering, absorption, and minority carrier extraction of 3D bulk heterojunction photovoltaic cells. Photovoltaic cells from domains with long and dense interpenetrating nanowire arrays improve the relative power conversion efficiency by 47% when compared to flat domains on the same substrate. We have not yet tested multiple parameters at a time but it should be possible to test other designs where the material is varied from one domain to the next, or where structures are formed that do not simply change the pitch or height. While the interpretation of the results would be more involved such an approach could lead to the discovery of new higher performance architectures.

4.4 Supplemental Informaion

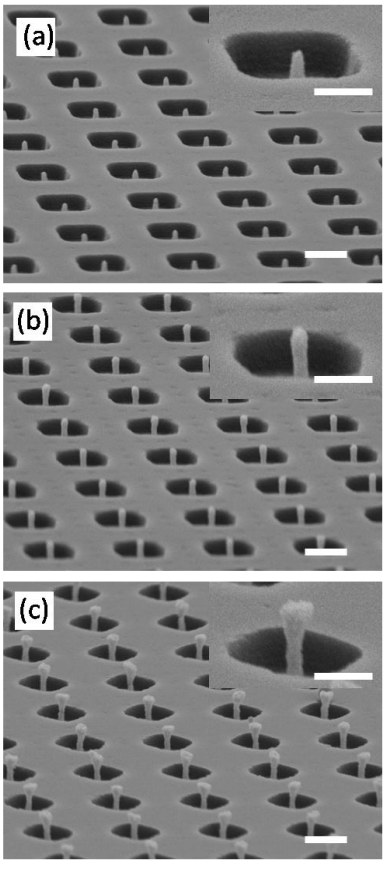

Figure 4-S1. *SEM of localized Pt deposits after (a) 40s, (b) 60s, and (c) 120s deposition time. 1 μm scale bars in (a-c) and 500 nm scale bars in the insets.*

Figure 4-S1 shows scanning electron microscope images of electrically controlled localized Pt deposits after (a) 40s, (b) 60s, and (c) 120s deposition time. The deposits are formed using an array of 1 μm wide and 500 nm deep holes in a Microposit S1805 photoresist which acts as a guide before the material reaches the biased ITO domain that is used to control the material flux. The material is funneled into a location which is roughly 10x smaller than the 1 μm wide opening itself leading to a diameter of 110 nm. The diameter of the nanowires begins to increase as they grow much taller than the photoresist guides themselves. For example after

deposition for 120s the structures have grown 1.5 µm tall which is 3 times the thickness of the 500 nm thin photoresist and the onset of broadening (mushrooming) becomes visible. As a design rule, structures will lack broadened tops if the deposition process is stopped before the towers significantly exceed the height of the photoresist film thickness itself.

The deposits shown in the manuscript are made out of very small, typically < 5 nm Pt, Ag and W single crystal particles, which were confirmed by analyzing the deposits using high resolution transmission electron microscopy (TEM) and energy dispersive x-ray spectroscopy (EDS). For completeness the data for tungsten is shown in Figure 4-S2**.** Platinum and silver were discussed in the main body.

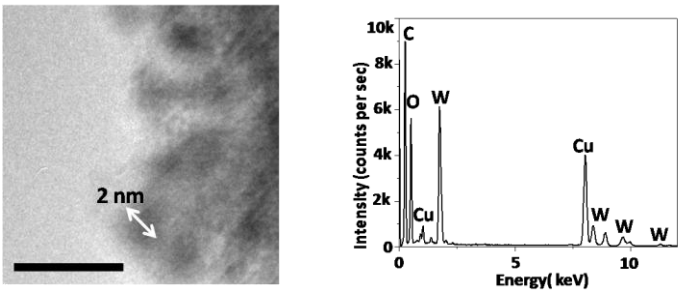

Figure 4-S2. *TEM and EDS data of tungsten particles. 5 nm scale bar.*

Figure 4-S3 shows the histogram with the measured variation in height in domain 5. The standard deviation (STD) was less than 13.1 nm for the 800 nm tall structures.

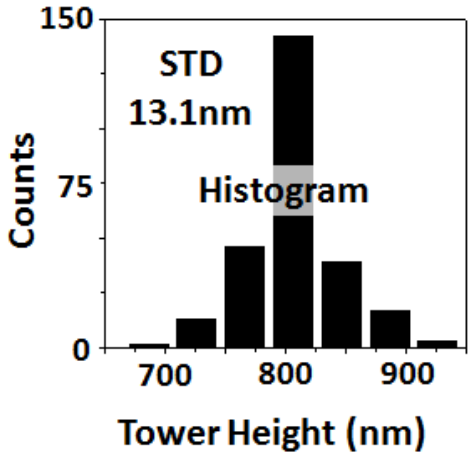

Figure 4-S3. *histogram of height that centers around 806 nm.*

Figure 4-S4 provides a larger area view of deposits after (a) deposition of Pt nanowires, (b) removal of photoresist guides, and (c) deposition of the thin film stack that is required to complete the solar cells. The completed device in (c) depicts about 1,000 deposition sites. Out of the 1,000 deposition sites, 5-6 sites are slightly elevated, and 1 site shows a defect where one of the 100 nm in diameter and 800nm tall nanowires is missing likely because it failed to withstand the spin coating step.

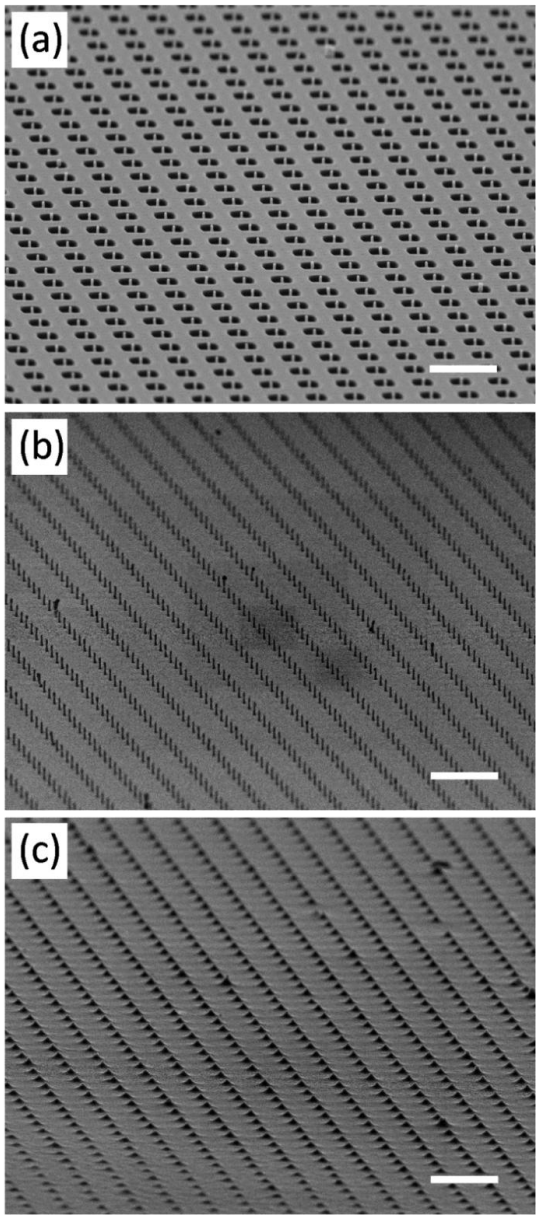

Figure 4-S4. *Large area views used to analyze defect rates after (a) deposition of Pt nanowires, (b) removal of photoresist guides, and (c) deposition of the thin film stack. 5 μm scale bars.*

Figure 4-S5 provides the photovoltaic cell processing steps, the final photovoltaic cells on 5 different domains and the energy level diagram. Figure 4-S5(a) shows the processing steps, the respective SEMs that are required to complete the devices. The steps are: 1. nanowire deposition using photoresist guides and bias control, 2. removal of the photoresist guides using an oxygen plasma, 3. spin coating of the electron blocking layer (PEDOT: PSS), active blend layer (P3HT: PCBM), and 4. vapor deposition of lithium fluoride (LiF) tunneling layer and aluminum top contact. Figure 4-S5(a1-a5)

showed the SEM images of the completed photovoltaic cells on five different domains and also depicted the respective short circuit current density for each domains. The energy level diagram and film thickness are illustrated in Figure 4-S5(b).

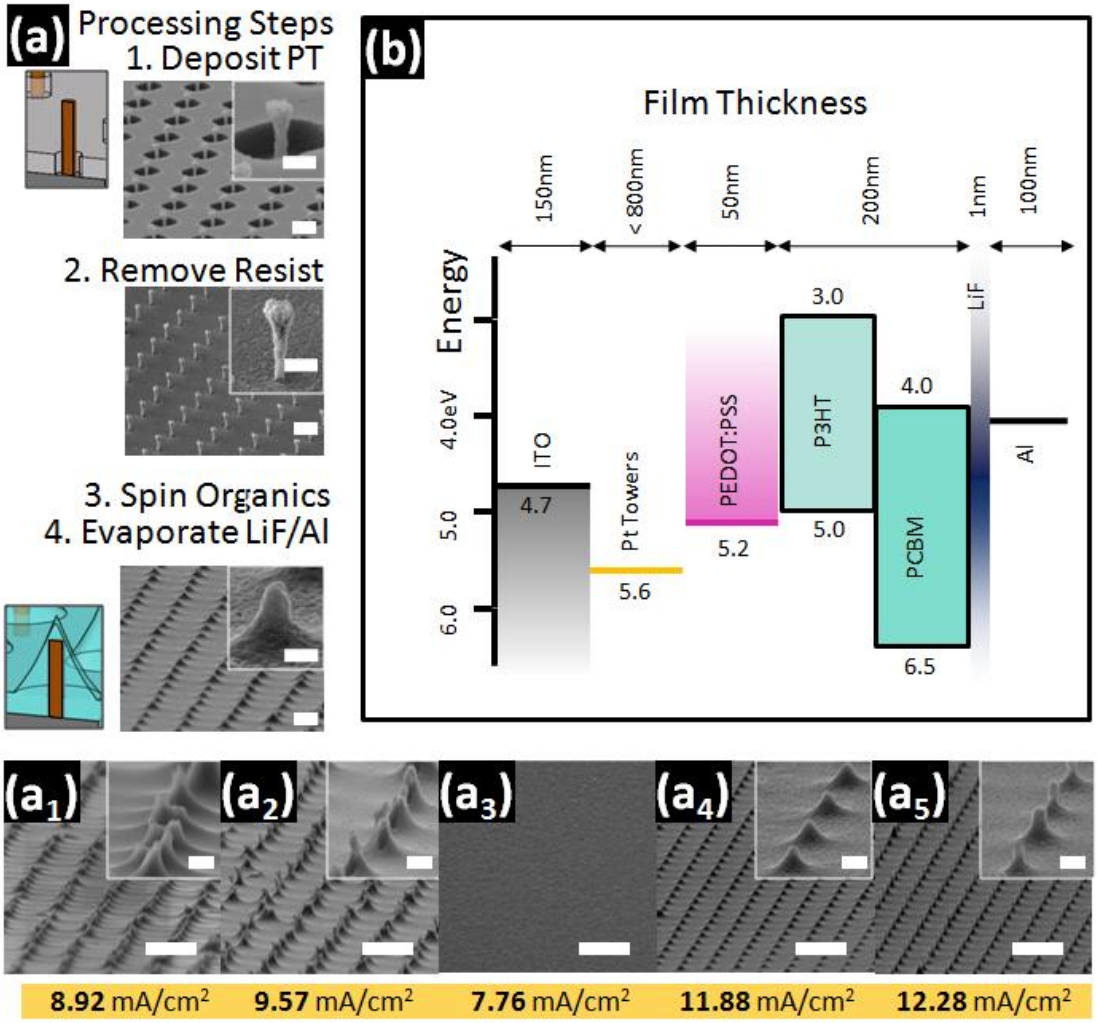

Figure 4-S5. *(a) Processing steps to complete the photovoltaic cells leading to the recorded short circuit current densities that improve for long and dense nanowire arrays. (a1-a5) The SEM images of complete photovoltaic cells in domain 1 to 5. (b) the energy level diagram and film thickness. 1 µm scale bars in (a). 300 nm scale bars in insets of (a). 5 µm scale bars in (a1-a5). 300 nm scale bars in insets of (a1)-(a5)*

Chapter V

Effective Localized Collection and Identification of Airborne Species through Electrodynamic Precipitation and SERS based Detection

En-Chiang Lin, Jun Fang, Se-Chul Park, Forrest W. Johnson, and Heiko O. Jacobs,

Reproduced with permission from:

Nature Communications (2013)

5.1 Introduction

Detection of chemical agents in the gas phase has attracted much attention due to the applications and potential for explosives detection and environmental monitoring[34, 41, 85, 86]. The detection of small molecules and airborne species at low concentration commonly requires sensing schemes where the analytes are absorbed on a surface. The process of absorption and precipitation is therefore critical to the detection limit of the analytes. This is true for all established gas phase sensing concepts including gas chromatography[28], ion mobility spectrometry (IMS)[29, 30], mass spectrometry[31], metal-semiconductor-metal-based sensors[32-34], chemical field effect transistors[35], nanocantilever[36], infrared detection[37], and surfaced-enhanced Raman spectroscopy (SERS)[38, 39]. Interestingly most of the more recently reported sensing schemes aim at increasing the sensitivity to a single molecular level[40] and use diffusion as a mechanism for transport which leads to a collection efficiency of the airborne species which is not optimized. Schedin *et al.*[40] as an example, reported the detection of a single molecule from a carrier gas at a concentration of 1 ppm. The experiments used a micrometer-sized graphene sensor. The authors concluded that "Large arrays of such sensors would increase the catchment area[87], allowing higher sensitivity for short-time exposures and the detection of active (toxic) gases in as minute concentrations as practically desirable." In other words, it becomes increasingly difficult to detect and capture molecules on the basis of diffusion in cases where the active sensing area is reduced unless the question of localized delivery is addressed. Effective collection on a small sensing area is not possible based on diffusion alone and the employment of a directed force will be required to solve the problem of transport. Both the thermophoretic and Coulomb force can be utilized to transport the analytes from a distance away to the sensing surface. At practical temperature gradients the thermophoretic force, however, remains low compared to concepts that use electrostatic precipitation[41]. Different from prior methods[28-33, 35-39] this article reports and applies a programmable localized electrodynamic precipitation concept to collect, spot, and detect airborne species in an active-matrix array like fashion. The approach discussed here does not use mechanical masks[42, 43] or high-precision contact-printing robots[44, 45] to deliver the analytes to desired points and provides programmability with a lateral resolution that is several

orders of magnitudes higher. Molecules of one type are directed from a space that is centimeters away to specific sensing regions and areas with 100 nm control over the lateral position and spot size. The detection scheme is demonstrated using a surface-enhanced Raman spectroscopy (SERS) sensitized nanostructured surface. It employs the standardized "Ag film over Nanosphere (AgFON) substrate"[38, 46] and compares the results with and without programmable localized electrodynamic precipitation and finds that SERS signals is enhanced by a factor of 615 comparing identical sensor surfaces. The process is able to detect charged benzenethiol molecules at an estimated level of 1.5 ppb (parts per billion) within 10 s; as a comparison, to detect uncharged molecules using a standard mechanism of diffusion a concentration of 6 ppm (parts per million) is required. The reported process is applied to produce hybrid molecular arrays on a single chip over a broad range of molecular weights including small molecules such as benzenethiol (110.18 Dalton) and 4-fluorobenzenethiol (128.17 Dalton) or large macromolecules such anti-mouse IgG proteins (~150k Dalton).

5.2 Results and Discussion

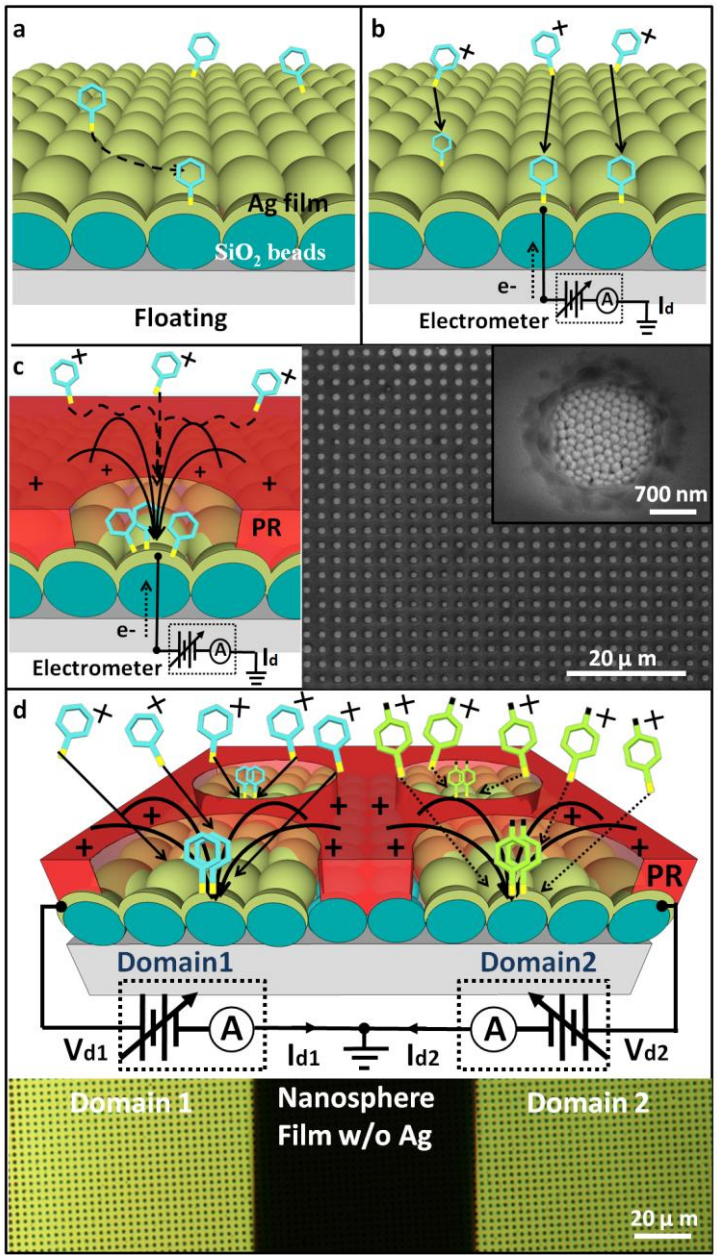

Figure 5-1 | Advanced collection, spotting and detection of airborne species for gas sensor applications comparing (a) diffusion, (b) a biased planar plate, (c) an electrodynamic nanolens enabled spotting concept, and (d) a programmable nanolens array. ***(a, b)*** *Depict a nanostructured substrate commonly used in SERS called Ag film over nanospheres (AgFON) which uses Ag coated SiO_2 beads[38, 46]; in* ***(a)*** *collection is*

*driven by diffusion, in (**b**) collection is driven by basic electrostatic precipitation through application of a bias voltage where I_d reflects the rate of charge dissipation. (**c**) The concept of electrostatic precipitation is enhanced using an electrodynamic nanolens approach; a nanolens is formed using a patterned photoresist layer (PR) to funnel, concentrate, and spot the molecules at predetermined locations while preventing deposition on the positively charged resist. (**d**) The concept is further enhanced using electrically separated domains to receive different analytes at different times; domains are programmed by applying an external bias voltage. Inserts in (**c**) and (**d**) depict SEM and optical microscope images of the corresponding test structures and dimensions that were used.*

Figure 5-1 depicts the investigated design elements and test structures which were evaluated to spot and collect airborne species on a nanostructured SERS gas sensor substrate. Figure 5-1a and b contrasts the state of the art diffusion based delivery concept with basic electrostatic precipitation where an external bias and charged molecules are tested to increase the collection efficiency. Figure 5-1c adds an additional design element -- a charged photoresist layer with a circular opening; the goal of this structure is to form an electrodynamic nanolens to funnel and concentrate the airborne species at a predetermined location on the nanostructured sensor surface. The use of a gas phase nanolens focusing effect has been reported recently in the context of inorganic nanoparticles[21-23, 88] which contained several 100,000 atoms which contrasts the small molecules tested here which contain less than 20 atoms. The general idea of a nanolens is to use a charged resist, which influences the trajectory of charged material. The resist is insulation and blocks charge dissipation. The opening to the conductor provides the only location where a charged material flux can be established under steady state conditions. Figure 5-1d depicts an additional modification to achieve programmability of more than one analyte. The approach uses electrically separated metallic domains (yellow cap layers) underneath the nanolens array.

The fabrication of the depicted test structures is detailed in the method section. In short, we used a Langmuir-Blodgett method[89] to apply a closely packed layer of silica spheres, 200 nm in diameter, over extended areas on the glass surface. Next, e-beam

evaporation is used to coat the top with 20 nm and 180 nm of chromium and silver, respectively. This yields the SERS sensing surface commonly known in the literature as AgFON standard. The silver film provides a conductive layer. This conductive layer allows for the application of an external bias voltage, which is used to evaluate if a field driven approach can increase the collection efficiency of charge molecules when compared to prior concepts[38, 39] where the rate of absorption was driven by diffusion and the substrate was left floating. Prior methods were able to detect benzenethiols at a concentration of 6 ppm in 1s. The second modification (Fig. 1c) adds the depicted 500 nm thick spin coated photoresist layer whereby a 1 µm in diameter and 3 µm pitched hole pattern is defined by photolithography. The final SERS gas sensor substrate (Fig. 1d) is composed of two silver domains instead of one. The two domains are separated using a 50 µm wide region of uncoated silica spheres which was masked by placing a capillary onto the surface prior metallization. All other parameters were left the same. The deposition on the individual domains is controlled using external bias voltages in the range of -50V to -200V whereby the electrometers records the deposition current in the range of 1 nA to 5 nA. The flux is recorded using electrometers (Keithley 6517A) marked with the letter "A". Domains are turned ON and OFF sequentially for selected periods of time (10 seconds to 1 minutes) to collect molecular ions including benzenethiol (BT^+) and 4-fluorobenzenethiol ($4\text{-}FBT^+$) on domain 1 and 2, respectively. We choose these two molecules since they have a well-characterized and known Raman scattering signal[38, 90]. The process is, however, not limited to these types of molecules or molecular weights. Results for anti-mouse IgG proteins (Sigma-Aldrich, F-0257) will be presented as well.

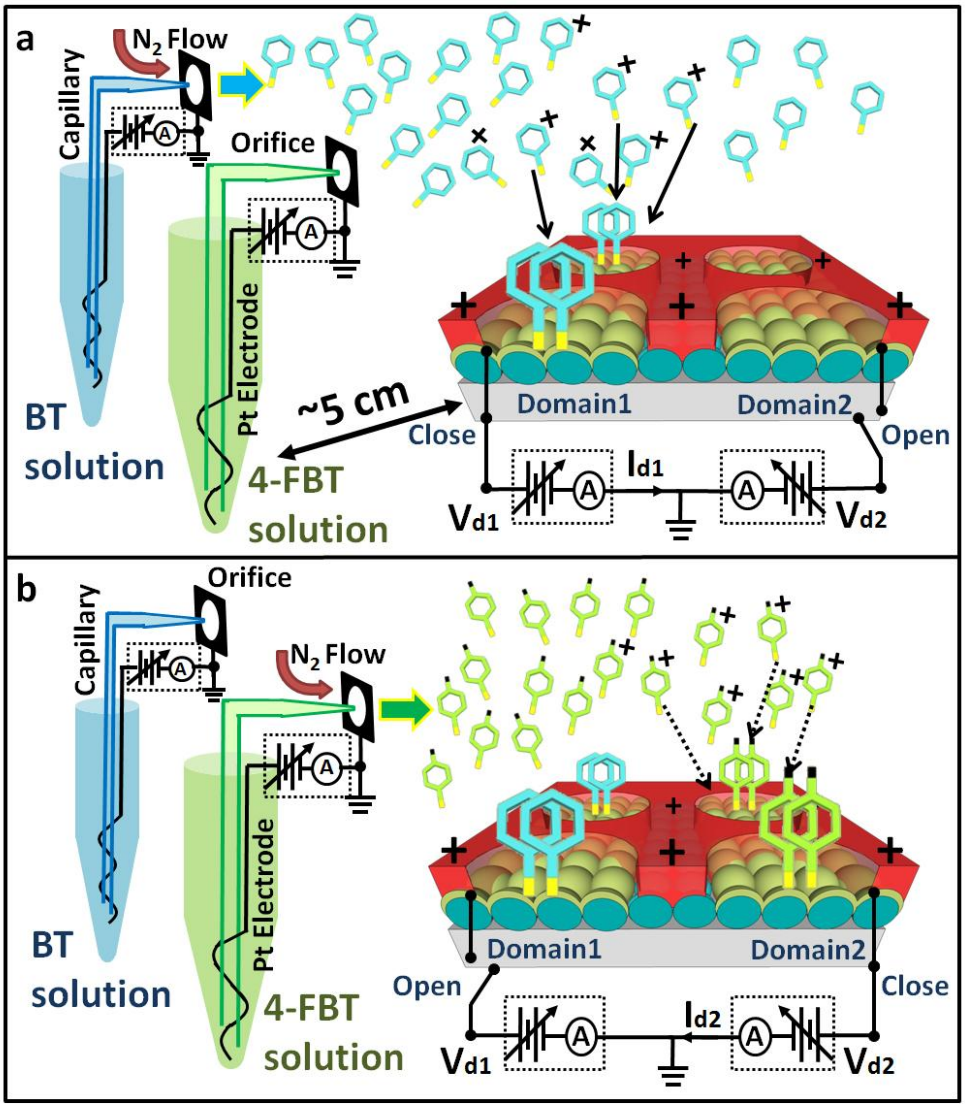

Figure 5-2 | Electrospray testing environment *depicting electrospray ionization to produce a flux of neutral and charged analytes where (**a**) benzenethiol (BT) ions shown in light blue are selected to deposit on domain 1 in step 1 and (**b**) fluorobenzenethiol (4-FBT) ions shown in light green are selected to deposit on domain 2 in step 2. Circular 1 µm in diameter openings in the positively charged photoresist layer (red) act as a nanolens array which concentrate the two analytes in predetermined sensing spots. The + sign on the red layer represents primary ionized carrier gas molecules. Switches marked as "open" and "close" are used to attract the analyte to the respective domains.*

Figure 5-2 depicts the details of the testing environment where the analytes are evaporated and charged using an electrospray ionization standard and where programmable analyte collection is achieved using biased domain electrodes. Electrospray ionization is chosen since it provides a controlled environment to produce airborne analytes of almost any type and concentration. Electrospray ionization systems are used in mass spectroscopy in the fields of chemical-warfare agent detection[91] and proteomics[92]. They require exceptionally small amounts of diluted analytes. For example at a common flow rate, only 50 nL is drawn through the capillary per minute. For a review, we refer to Cloupeau and Prunet-Foch[93] and Ganan-Calvo *et al.*[94]. In brief, we constructed a system based on a commercially available electrospray ionization system (TSI Inc., Model 3480). It consists of a high-voltage source, pressure regulator, pressure chamber, capillary, and electrospray chamber. The pressure chambers house a centrifuge vial, a high-voltage platinum electrode, and a fused silica capillary which carries the solution out into the electrospray chamber using 1.25 atm pressure. A positive electrospray voltage is increased until the extruded liquid (50 nL/min) forms a cone shape, known as cone-jet mode[95], which leads to rapid evaporation in close proximity to the orifice and an aerosol containing charged molecules (light green for 4-fluorobenzenethiol, and light blue for benzenethiol).

Figure 5-2a depicts the first analyte collection sequence where benzenethiol ions (BT^+) are collected on domain 1 which is turned ON by applying a negative voltage V_d= -100 V to the domain electrode. Domain 2 is switched into a floating state whereby the domain electrode is disconnected to prevent dissipation of charge which in turn blocks the collection on domain 2. The following conditions were used to prepare the depicted ionized aerosol containing charged benzenethiols. The starting point is a benzenethiol solution (liquid density=1.073 g/mL, molecular weight=110 g/mol) which is diluted in a 1:1 volume ratio with ethanol; second the solution is sprayed at a rate of 50 nL/min which translates to 2.43×10^{-7} N_A benzenethiol molecules per minute where N_A is Avogadro's constant; third it is mixed with 1L/min nitrogen carrier gas at 1.25 atm adding 4.1×10^{-2} N_A nitrogen molecules/min to the mixture; at this stage the analyte is diluted down to 5.9 ppm. In positive ion mode the process produces in addition to neutral molecules, positively charged molecules[96]. Of importance are benzenethiol ions ($C_6H_5SH_2^+$), 4-

fluorobenzenethiol ($C_6H_5FSH^+$), solvent ions ($C_2H_5OH_2^+$), and nitrogen ions (N_2^+). Figure 5-2b illustrates a second analyte collection sequence where fluorobenzenethiol (4-FBT^+) is collected on domain 2 and where domain 1 is left floating. The preparation approach for 4-fluorothiophenol (4-FBT) followed the same procedure as described before in the case of benzenethiol. The illustration in Figure 5-2 underrepresents the amount of neutral species for clarity. However, it is important to mention that most gas molecules are neutral and that the fraction of charged material is small. For example, a typical electrospray current is 100 nA which is measured using the ampere meter marked with the letter "A" that is connected to the platinum electrode that is immersed in the vial; 100nA electrospray current translates into an ion current flux of 6.23×10^{-11} N_A elementary charges per minute. This ion flux is three orders of magnitudes smaller than the previously calculated 2.43×10^{-7} N_A benzenethiol molecules and nine orders of magnitudes smaller than 4.1×10^{-2} N_A nitrogen gas molecules contained in 1L/min carrier gas. In other words the gas mixture is composed of both charged (<1.5 ppb) and neutral benzenethiol (<5.9 ppm) molecules. The gas mixture exits the enclosed system through a 0.5 mm in diameter orifice and expands until it reaches the substrate, which is placed 5 cm away. The ppb and ppm estimates are upper limits and the actual concentration of charged and neutral molecules is smaller due to downstream mixture and charge exchange processes which will be discussed further in the discussion section.

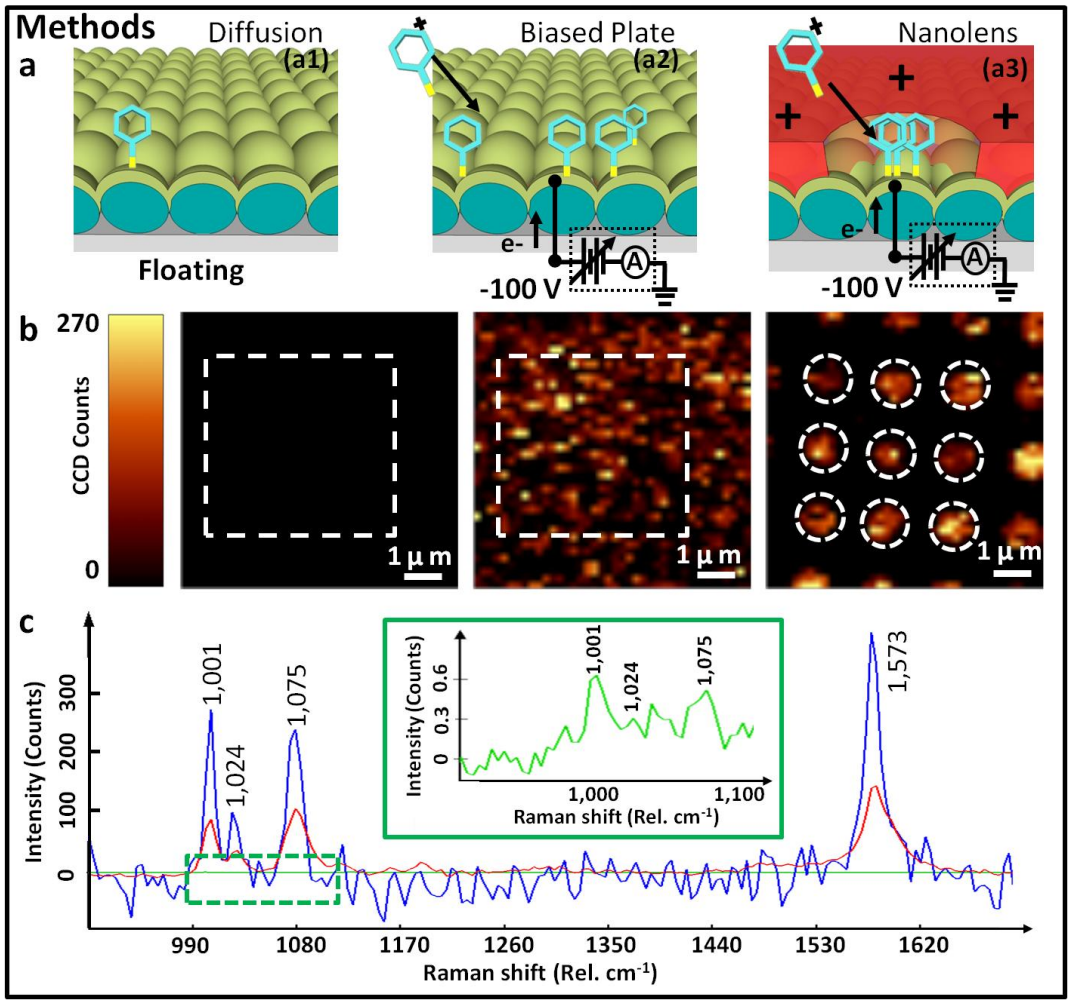

Figure 5-3 | Schematics and experimental results comparing analyte collection based on diffusion (LEFT), a biased plate (CENTER), and a nanolens based collection concept (RIGHT) using a constant 30s long exposure *to a gas mixture containing both charged and neutral benzenethiols. The biasing conditions depicted in (a) lead to (**b**) the recorded scanning confocal Raman intensity map of the characteristic Raman peak at 1,075 cm^{-1} and (**c**) corresponding spectra where the signal intensity for the biased substrates improves by a factor of 615.*

Figure 5-3 compares the recorded SERS signals using the floating, biased plate, and biased nanolens collection approach after the test substrates were exposed for 30 s. The gas mixture exiting the electrospray system containing both charged (<1.5 ppb) and neutral benzenethiol (<5.9 ppm) molecules in nitrogen. All SERS spectra in Figure 5-3c

were recorded under identical exposure and recording conditions which is important as this allows a relative comparison of the signal intensity for a sensor system with and without charge directed collection. For a standard SERS substrate hotspots are randomly located on the surface (Figure 5-3b) and it is hard to point out where the molecule is. The nanolens based collection approach eliminates this uncertainty since molecules are collected at predetermined points (Figure 5-3c). This helps in the data collection. In the particular case all SERS spectra were recorded as an average over the indicated white dashed areas; no voltage is applied during the recording of the SERS data. The spectrum for the unbiased case shows a weak signal and the detection of the uncharged benzenethiol is difficult at 6 ppm in our system; the characteristic peak at 1,075 cm^{-1} is recorded with 0.4 counts per unit area (inset of Figure 5-3c) which means very few benzenethiol molecules are collected on this substrate. The signal increases to 103 counts per unit area for the biased AgFON substrate and 246 counts per unit area for the biased AgFON substrate with integrated nanolens array which represents a factor of 615 comparing the biased nanolens array with the unbiased AgFON standard. We repeated this experiment five times using separate substrates. The nanolens-based collection region produced the highest counts in each case; the intensity factor varied by 6% (STD) between experiments. The recorded increase of 615 is even more impressive if one considers that it is caused by 3,900 times fewer charged analyte molecules (1.5 ppb) than neutral ones (5.9 ppm). In other words trace amounts of charged molecules at a concentration of 1.5 ppb (parts per billion) lead to 246 counts per unit area while 5.9 ppm (parts per million) of neutral particles contribute to 0.4 counts which means that the capture efficiencies of charged molecules is 2.4×10^6 times larger than neutral ones. The six orders of magnitude higher capture efficiencies of charged molecules when compared to neutral one is an important metric since it provides a route to higher sensitivity in any gas sensor application that presently uses diffusion as a mechanism of transport. Adding additional system components to charge the analyte to assist collection should yield similar gains.

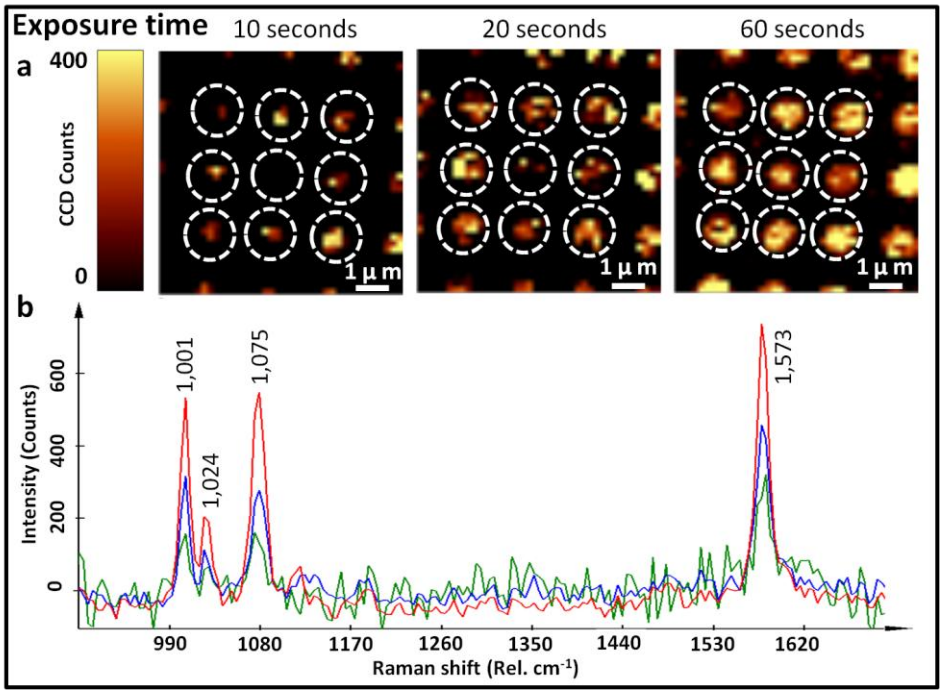

Figure 5-4 | SERS images (a) and spectra (b) for the localized nanolens enabled collection approach *testing different collection times: 10 s (LEFT, green line), 20 s (CENTER, blue line), and 60 s (RIGHT, red line).*

Figure 5-4a,b depict the Raman microscopy intensity map at 1,075 cm^{-1} Raman shift and spectra for the nanolens enabled collection approach as a function of collection time. The nanolens approach supports a more automated image processing which enables the elimination of the searching and hand picking of hotspots which is a common practice in SERS related measurements. Instead, we used a standard array of detection windows outlined with the dashed lines and averaging over these areas to record the spectra. The characteristic peaks at 1,001 cm^{-1}, 1,075 cm^{-1}, and 1,573 cm^{-1} begin to emerge after a 10 s long exposure to charged benzenethiols. For short periods of time the signal increases roughly linear with exposure time and begins to level off after 60 seconds. For example, counts at the 1,001 cm^{-1} Raman shift are 170 (1x), 320 (1.9x), 540 (3.2x) for 10s, 20s, 60s, respectively. This non-linear behavior and saturation for prolonged capture times can be explained by excessive packing of molecules which are not as tightly coupled to the plasmonic surface[97]. For the same reason the signal-to-noise-ratio increases at first with exposure time before it levels off.

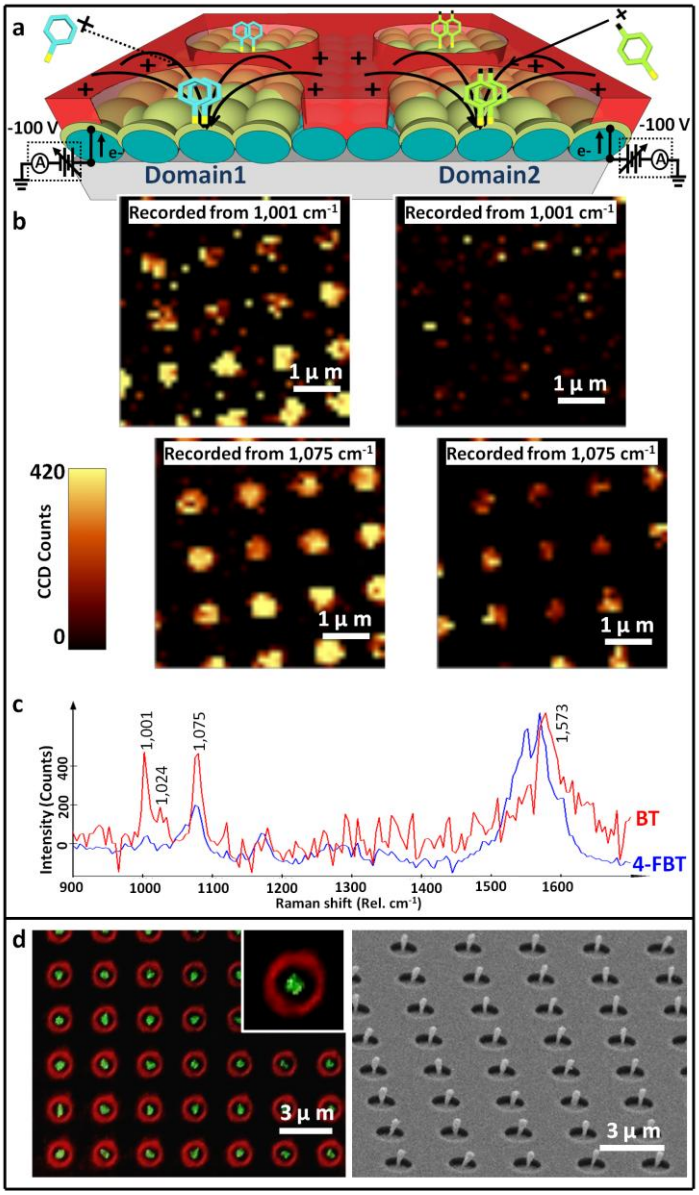

Figure 5-5 | Schematics and experiment results to spot and detect different molecules on a single substrate using programmable domain electrodes. *(**a**) Schematic details the collection and SERS based detection of benzenethiols on the left and 4-fluorobenzenethiols on the right. (**b**) Associated confocal Raman microscope intensity maps at wavenumbers 1,001 cm^{-1} and 1,075 cm^{-1} next to the (**c**) corresponding SERS spectra. (**d**) The fluorescent microscopy image shows the green fluorescence of large macromolecular anti-mouse IgG proteins which are funneled into the photoresist hole pattern.*

Figure 5-5 illustrates experimental results where programmable domain electrodes are used to spot different molecules with different molecular weights, specifically benzenethiol (110.18 Dalton), 4-fluorobenzenethiol (128.17 Dalton), and anti-mouse IgG (~150k Dalton). The small molecules displayed characteristic Raman peaks which enable the recognition in the anticipated domains. As an example, domain 1 shows the presence of a peak at 1,001 cm^{-1} which is known to be a dominant peek for the benzenethiol which is not the case in 4-fluorobenzenethiol in domain 2. Both molecules share a peak at 1,075 cm^{-1} which represents a stretching mode of the aromatic ring. We would like to note that the intensity of the SERS signal depends on both the analyte amount and the localized plasmonic resonance. Plasmon resonances will only occur in the Ag layer and not on the photoresist surface. In other words, the absence of a SERS signal on the photoresist surface is not sufficient to conclude that there are no molecules on the photoresist. The previously presented increases in signal counts by a factor of 615 (Figure 5-3) comparing the biased nanolens array with an unbiased surface can, however, only be explained by an increased localized collection process. To further validate that material is only collected in the opening we decided to use a fluorescence-based detection scheme and a much larger molecule in hope to image the location [98] using fluorescence microscopy. Specifically we tested anti-mouse IgG which is tagged with conventional fluorescence markers (fluorescein isothiocyanate, green). Figure 5-5d depicts the results. The fluorescence based detection scheme decouples the detection mechanism from the plasmon resonant Ag layer. The intensity of the green fluorescence on the Ag surface and absence of fluorescence on the photoresist surface can now be used as a measure of the selectivity with which the localized analyte delivery takes place. No detectable quantities of the IgG molecules are found on the photoresist and collection is observed only in the center of the opening. Moreover, because IgG is three orders of magnitudes larger than the thiol molecules in this study it was possible to resolve the location of physical analyte collection by SEM. The molecules are confined to a 200 nm in diameter region which is smaller than the 1 μm in diameter opening.

5.3 Conclusion

Various nanostructured sensors currently aim to claim single molecular detection by a reduction of the active sensor size. An equally important challenge, however, can be found in the question “whether the analyte will find the nanometer sized surface”. The reduction in the size of the active sensor will ultimately require research on methods which enable localized delivery. The reported electrodynamic collection concept is a first step in this direction. The process can be applied to small and large molecules of almost any type as long as they can be charged. The use of electrodynamic forces benefits from unique scaling laws which can be both long range using parallel plates and highly localized with sub 100 nm confinement using simple patterned insulating resists that can be charged to guide the analyte to specific locations. This is our view which is not possible with any other method. While the collection and spotting were demonstrated using surface-enhanced Raman spectroscopy and fluorescence based markers the localized gas phase analyte deliver method should be applicable to other sensing concepts. The relative sensitivity increases in the case of the SERS sensor was 615 comparing the biased nanolens array with the unbiased AgFON standard. The value has not be optimized and is based on the 1 μm in diameter and 3 μm pitched hole pattern shown in Figure 5-1; higher values can be anticipated but would require optimization of the opening size, pitch, domain size, and domain potential. Most interesting, however, is the fact that the gas mixture contained far less charged (<1.5 ppb) analyte molecules than neutral ones (<5.9 ppm); in other words the inability to detect the neutral molecules despite the fact the concentration was 4 orders of magnitude larger than the charge molecules motivates the anticipated gains of incorporating advanced charging concepts from a sensor system point of view. Many gas sensor systems currently use diffusion as the only mechanism of transport and dramatic improvements can be anticipated incorporating various forms of localized delivery which would impact environmental monitoring systems or the detection of chemical or biological warfare agents. The reported process can also be used as a programmable selected area deposition or surface treatment method with molecular ions. The sequence and amount can be mixed and matched with a lateral resolution that is several orders of magnitudes higher than what is possible using existing methods that are based on mechanical shutters or high-precision

contact-printing robots. The ability to fabricate hybrid molecular arrays with control over material sequence, composition, and lateral distribution on a single substrate within a single process could potentially be used in other applications which include, proteomics and cell research, pharmaceutical screening processes, panel immunoassays, and molecular electronics[44, 45, 99].

Chapter VI

Effective Collection and Detection of Airborne Species Using SERS Based Detection and Localized Electrodynamic Precipitation

En-Chiang Lin, Jun Fang, Se-Chul Park, Thomas Stauden, Joerg Pezoldt and Heiko O. Jacobs,

Reproduced with permission from:

Advanced Materials (2013)

6.1 Introduction

Detection of airborne species has attracted much attention due to the applications and potential for explosives detection and environmental monitoring[34, 41, 85, 86]. The detection of chemical agents commonly requires sensing schemes where the analytes are absorbed on a surface. The process of transport, absorption and precipitation is therefore critical to the detection limit of the analytes. This is true for all established gas phase sensing concepts including gas chromatography[28], ion mobility spectrometry (IMS)[29, 30], mass spectrometry[31], metal-semiconductor-metal-based sensors[32-34], chemical field effect transistors[35], nanocantilever[36], infrared detection[37], and surface-enhanced Raman spectroscopy (SERS)[38, 39].

Recently Schedin et al. reported gas molecule detection with a sensitivity down to a single molecular level[40] and used diffusion as a mechanism for transport. While the results are impressive the use of diffusion may not be the best approach since it leads to a collection efficiency of the airborne species which is not optimized. In other words, single molecular detection sensitivity is important but requires the molecule of interest to reach the sensing surface with maybe sub 100 nm in size. Effective collection on a small sensing area is not possible based on diffusion alone and the employment of a directed force will be required to solve the problem of transport.

This transport problem could be addressed for example using thermophoretic and Coulomb forces to transport the analytes from a distance away to the sensing surface. At practical temperature gradients the thermophoretic force, however, remains low compared to concepts that use electrostatic precipitation[41]. Different from prior methods[28-33, 35-39] this article reports and applies a localized electrodynamic precipitation concept to collect, spot, and detect airborne species. Molecules are directed from a space that is centimeters away to specific sensing regions and areas with 100 nm control over the lateral position and spot size. The detection scheme is demonstrated using a surface-enhanced Raman spectroscopy (SERS) sensitized nanostructured surface including the standardized “Ag film over Nanosphere (AgFON) substrate”[38, 46]. In total this study compares three different analyte delivery concepts (standard diffusion, global electrodynamic precipitation, and localized nanolens based precipitation) and three different SERS enhancement layers (a flat silver film, a nanolens enabled localized

deposited film of silver nanoparticles, and the standard AgFON surface layer). The electrodynamic nanolens array reported here is a new design element. The nanolens array enables us to funnel and concentrate the airborne analyte molecules to discrete sensing points with sub 100 nm lateral resolution. The introduction of this concept had the biggest impact in terms of increasing the SERS signal intensity; a factor of 633 when compared to a standard mechanism of diffusion was observed. The nanolens array was also used to direct the precipitation of Ag nanoparticles to prepare a SERS enhancement layer which performed equally well as the (AgFON) standard.

6.2 Results and Discussion

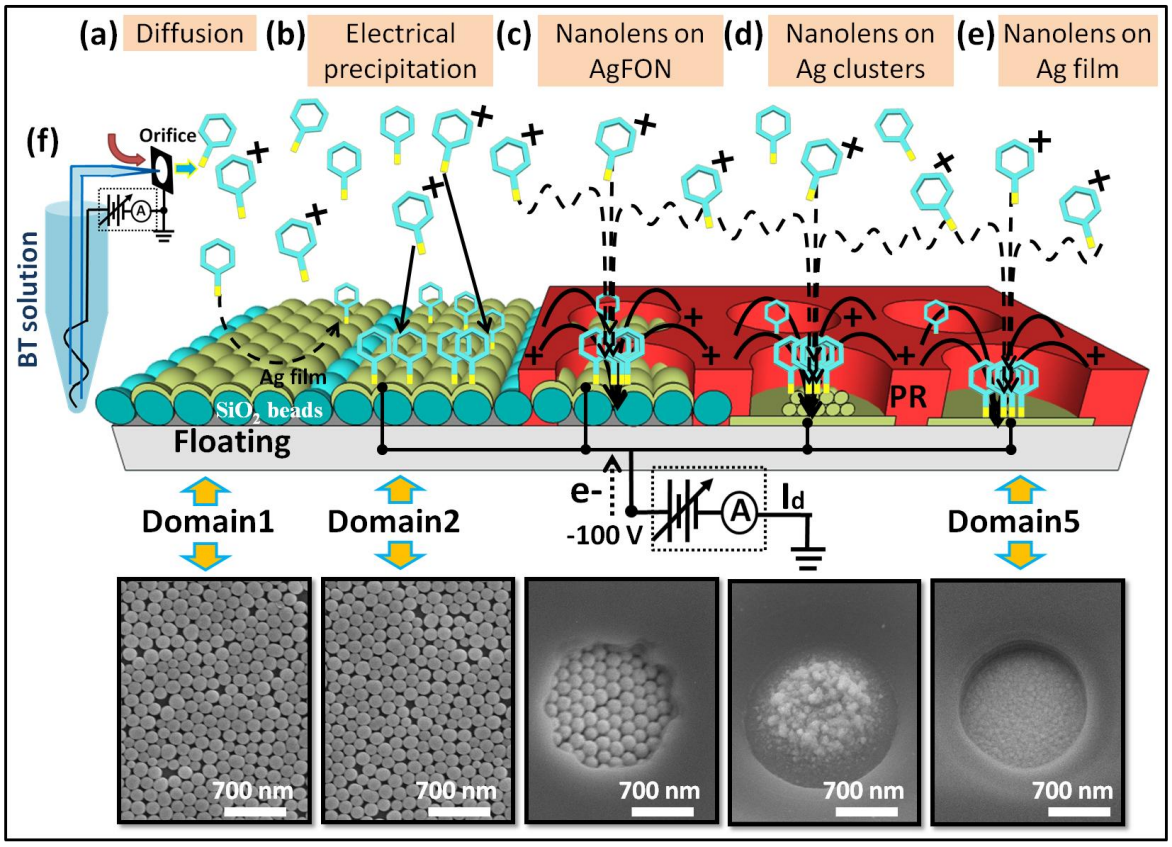

Figure 6-1. | Methods and test samples employed to evaluate and demonstrate advanced collection, spotting, and detection of airborne species testing three different delivery mechanisms (a, b, c) and three different SERS nanostructured surface layer designs (c, d, e) on a single substrate. *(a) Schematic depicting that a portion of the analytes attach to the Ag coated SERS surface on the basis of diffusion (domain 1). (b) A*

fraction of the anayte is charged but are captured in greater numbers through application of a bias to the conducting AgFON domain (domain 2). (c) A nanolens array composed of 1 μm in diameter openings inside a 500 nm thick positively charged resist is used to funnel the charged analyte to predetermined locations leading to a locally enhanced concentration (domain 3). The AgFON standard composed of Ag coated 200 nm in diameter closed packed silica beads was used in domain 1-3. (d) The same nanolens based collection is maintained but the AgFON sensor surface is replaced with localized aggregated (5-10 nm) Ag particles forming a 250 nm think deposit on a biased flat silver layer (domain 4), and (e) a biased flat silver domain provides a reference (domain 5). The SEM micrographs depict the actual structure that were used in the experiments. (f) Testing environment depicting electrospray ionization to produce a flux of neutral and charged analytes of known concentration.

Figure 6-1 details the delivery methods and test structures employed to evaluate and demonstrate advanced collection, spotting, and detection of airborne species testing three different delivery mechanisms (a, b, c) and three different SERS nanostructured surface layer designs (c, d, e). Domain 1 depicts the conventional concept of diffusion-based collection utilizing a conducting AgFON "SERS standard" sensor surface. This represents the state of the art and experimental approach that is commonly used. Airborne analyte molecules such as the depicted benzenethiols molecules attach to the surface over time on the basis of diffusion. However, aerosols always contain a fraction of charged species. While this fraction is commonly at least of factor of 1000 smaller than neutral particles it might be possible to manipulate these far fewer molecules more effectively which is explored in this study through the application of an external potential to electrically separated domain electrodes labeled as domain 2-5. Domains 3-5 also use the application of an external bias voltage but add a localized electrodynamic collection approach whereby a nanolens is formed using a patterned positively charged photoresist layer (PR) to funnel, concentrate, and spot charged molecules to predetermined locations. The general idea of a nanolens is to use a charged resist, which influences the trajectory of charged material. The resist is insulation and blocks charge dissipation. The opening to the biased domain electrode provides the only location where a charged material flux can be established under steady state conditions. This approach is a novel design element

since it achieves localized collection of charged analyte molecules at a higher level of concentration than otherwise possible. While domains 3-5 use the same nanolens directed collection approach the SERS sensor surfaces is adjusted to be different: (c) depicts the AgFON "SERS standard" composed of Ag coated 200 nm in diameter closed packed silica beads, (d) a SERS surface layer composed of localized aggregated (2-5 nm) Ag particles forming a 250 nm thick deposit, and (e) a SERS reference layer composed of a bare and flat 150 nm thick silver surface which provides another reference. The inserted SEM micrographs next to the schematics show the actual dimensions of the fabricated test structures.

To test this substrate and collection concepts we used a commercially available electrospray system (TSI Inc., Model 3480) which is capable of preparing various aerosols containing a known composition of charged and neutral analyte molecules (Fig. 1f) . In brief the system consists of a high-voltage source, pressure regulator, pressure chamber, capillary, and electrospray chamber. The pressure chambers house a centrifuge vial, a high-voltage platinum electrode, and a fused silica capillary which carries the solution out into the electrospray chamber using 1.25 ATM pressure. The following conditions were used. A positive electrospray voltage is increased until the extruded liquid (50 nL/min) forms a cone shape, known as cone-jet mode[95], which leads to rapid evaporation in close proximity to the orifice and an aerosol containing charged molecules (used light blue for benzenethiol in Figure 6-1). In positive ion mode the process produces in addition to neutral molecules, positively charged molecules[96]. Of importance in our experiment are benzenethiol ions ($C_6H_5SH_2^+$), solvent ions ($C_2H_5OH_2^+$), and nitrogen ions (N_2^+).

In the experiments we used a benzenethiol solution (liquid density=1.073 g/mL, molecular weight=110 g/mol) which is diluted in a 1:1 volume ratio with ethanol; second the solution is sprayed at a rate of 50 nL/min which translates to $2.43*10^{-7}$ N_A benzenethiol molecules per minute where N_A is Avogadro's constant; third it is mixed with 1L/min nitrogen carrier gas at 1.25 ATM adding $4.1*10^{-2}$ N_A nitrogen molecules/min to the mixture; at this stage the analyte is diluted down to 5.9 ppm. Charging occurs as a result of the electrospray process and the amount of charge can

calculated directly from the electrospray current. All experiments were conducted using a typical electrospray current of 100 nA which represents an ion current flux of $6.23*10^{-11}$ N_A elementary charges per minute. In relative terms these numbers translate to a gas mixture which is composed of approximately 1.5 ppb charged molecules (calculated using $6.23*10^{-11}$ N_A charged molecules in $4.1*10^{-2}$ N_A nitrogen molecules) and 5.9 ppm neutral benzenethiol molecules (calculated using $2.43*10^{-7}$ N_A benzenethiol molecules in $4.1*10^{-2}$ N_A nitrogen molecules). The given values are upper limits since it does not include downstream mixture and charge exchange reactions before the mixture reaches the substrate that is placed 5 cm away from the nozzle.

The guided nanolens assisted deposition process depicted in (Fig. 1c-e) should be considered as an electrodynamic process since the field distribution evolves over time. In the initial stages of the experiment ions respond to the external bias voltage. The smallest ions N_2^+ have the highest mobility and arrive first at the sample surface. This transient response results in a sheath of space charge on the sample surface depicted as ”+” on the red colored photoresist layer which alters the potential distribution. The potential distribution equilibrates and leads to a potential funnel where the analyte deposits in the center of the opening. Steady state charge dissipation can only occur in the opening and leads to a measurable flux of positive gas ions which includes the targeted molecules under a negative substrate bias of -100 V and this flux can directly be recorded using electrometers (Keithley 6517A) marked with the letter “A”.

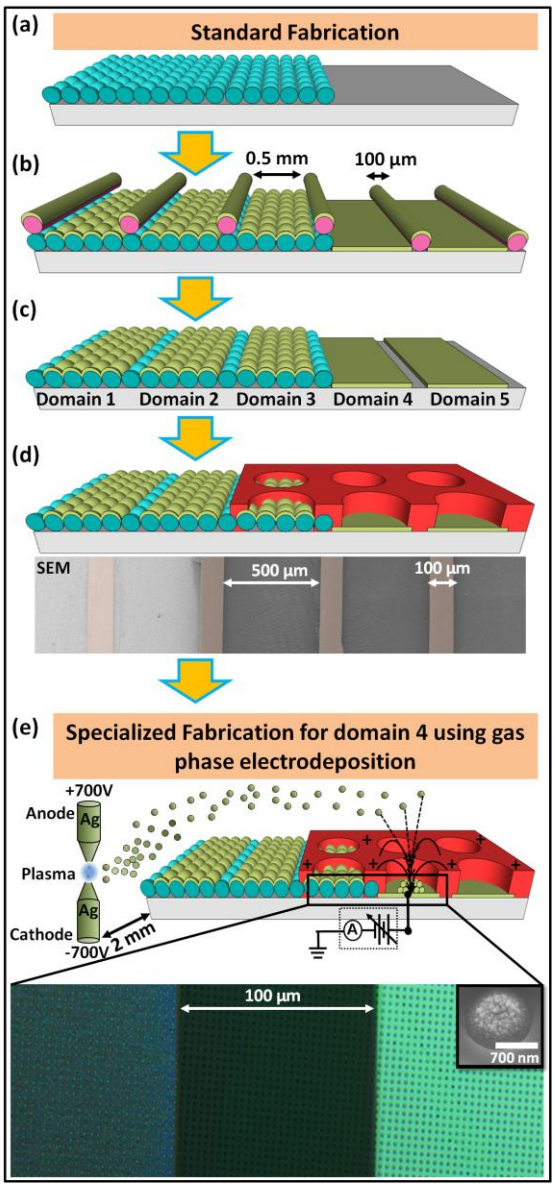

Figure 6-2. | Schematics and micrographs detailing the fabrication of a programmable SERS substrate for advanced collection, spotting and detection of airborne species. *(a) 200 nm silica nanospheres are locally assembled on a glass slide to form a closely packed layer of nanospheres. (b,c) 20 nm chromium and 150 nm silver film are evaporated on substrates and partially masked using 100 µm in diameter capillaries. (d) Photolithography is used to prepare 1 µm in diameter holes on top of domain 3-5. (e) Gas phase electrodeposition[21-23] is used to selectively deposit localized aggregated (2-10 nm) Ag particles in the openings on domain 4. Inserts in (d, e) depict SEM images and optical microscope images of the corresponding test structures and dimensions that were used.*

A goal was to prepare a single substrate with different domains and reference structures to aid in the comparative study of the design elements and to help get conclusive results. Figure 6-2 depicts fabrication details of the investigated designs. The supplemental information section provides additional information on the materials. The preparation followed these steps: Glass slides were pretreated in piranha etches at 120 ℃ for 30 min and treated in 5:1:1 ratio of H_2O:NH_4OH:H_2O_2 for 30min to make the surface hydrophilic. Monodisperse silica nanospheres (200 nm in diameter) were assembled into a closely packed layer onto a portion of the substrate through drop coating using 4% silica spheres by weight in water further diluted in ethanol (1:1 volume ratio) to aid in the spreading (Fig. 2a). We used 20 nm and 150 nm e-beam coated chromium and silver, respectively, and hand placed 100 ・ m in diameter capillaries to fabricate 5 electrically isolated domains on a single substrate (Fig. 2b,c). The depicted metal coated silica spheres are known in the literature as "AgFON SERS standard"[38, 46]. The silver film provides a conductive layer. This conductive layer allows for the application of an external bias voltage, which is used to evaluate if a field driven approach can increase the collection efficiency of charge molecules when compared to prior concepts where the rate of absorption was driven by diffusion and where the substrate was left floating[38, 39]. Domains 3-5 were further modified through integration of a photoresist based nanolens array (Fig. 2d) using a 500 nm thick spin coated photoresist layer (Microposit S1805) which was patterned using photolithography to define a 1 μm in diameter and 3 μm pitched hole pattern. The SEM image depicts the actual test structure and dimensions that were used.

The last step applies a thin layer of silver nanoparticles to domain 4 (Fig. 2e). The modification of domain 4 is not a standard vapor phase coating process since it applies the nanoparticles only to a selected domain. This particular process has only been reported recently in the literature[21-23]. It was referred to as gas-phase electrodeposition since it used charged nanoparticles in a carrier gas that can be applied locally through application of an external bias voltage[21-23]. The referenced results motivated this research since it reported surprisingly high deposition rates despite the fact that only a small fraction of particles were charged which at first seemed a contradiction. Anyway, here it is used to locally deposit (2-10 nm) Ag particles on domain 4 through application

of a negative bias voltage of 150 V yielding a 200 nm thick aggregated layer of Ag nanoparticles in 60 seconds at 100 °C only on the biased domain. The supplemental section provides a TEM microscope image which reveals the size of the primary particles. The origin of the charged particles is a confined “DC arc discharge based plasma” which uses two consumable electrodes. Experimentally we used the following conditions: 0.5 mm spaced silver electrodes, a discharge current of 100 mA in air at 1ATM, and a distance of 2 mm to the nearby substrate. The actual appearance of the localized nanoparticles is shown in the SEM (insert) whereby the optical microscope images provides an overview of the corresponding test structures with the relevant dimensions of domain 3 and 4.

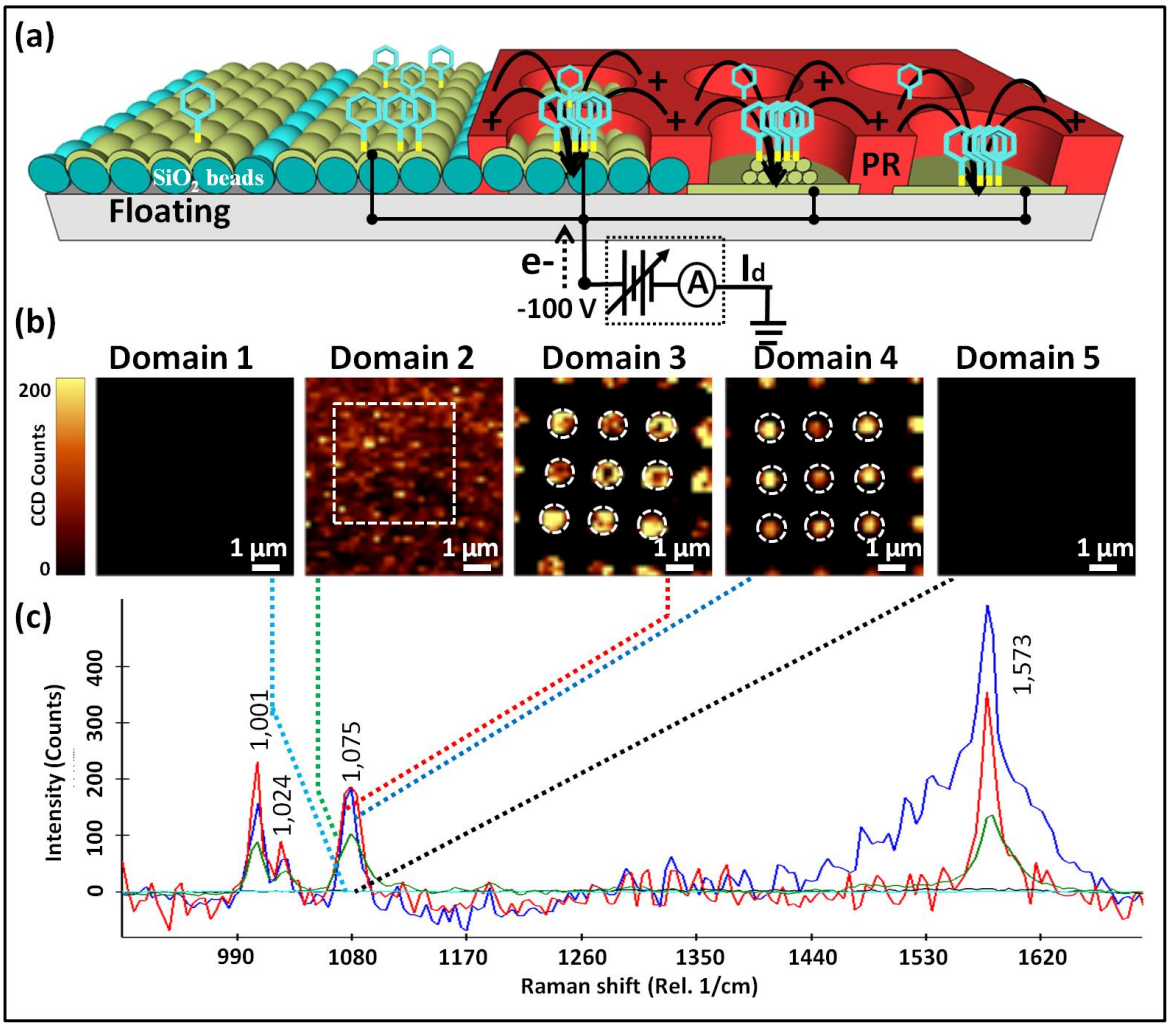

Figure 6-3 | Schematics (a), with corresponding scanning confocal Raman microscopy intensity map (b), and spectra (c), comparing different delivery methods and SERS sensor designs on a single substrate which is exposed to a gas mixture containing both charged (<1.5 ppb) and neutral benzenethiols (<5.9 ppm) for 20s. *The results represent standard diffusion (Domain 1), a biased region (Domain 2), a nanolens enabled molecular spotting approach integrated on top of: a AgFON SERS standard layer (Domain 3), a localized Ag nanoparticle layer (Domain 4), and a flat silver film (Domain 5).*

Figure 6-3 compares the recorded SERS signals testing a 20s long exposure to the gas mixture containing charged (<1.5 ppb) and neutral benzenethiol (<5.9 ppm) molecules in nitrogen. The actual biasing conditions are depicted in Figure 6-3a. The resulting intensity map (Fig. 3b) of the Raman peak at 1,075 cm^{-1} and the SERS spectra (Fig. 3c) were recorded using identical recording conditions. The spectrum for the unbiased case shows a weak signal and the detection of the uncharged benzenethiol was difficult at 6ppm; the characteristic peak at 1,075 cm^{-1} is recorded with 0.3 counts per unit area which means very few benzenethiol molecules are collected on this substrate. The signal increases to 103 counts per unit area for the biased AgFON substrate and 190 counts per unit area for the biased AgFON substrate with integrated nanolens array which represents a factor of 633 comparing the biased nanolens array with the unbiased AgFON standard. The result is particular intriguing if one considers that we had at least 3 orders of magnitudes less charged benzenethiols (<1.5 ppb) in the gas mixture than neutral ones (<5.9 ppm). Or in other words trace amounts of molecules at a concentration of 1.5 ppb can be detected in 20s as long as they are charged which is not possible using a standard mechanism of diffusion where a concentration of 6 ppm is required to get above the noise level of the instrument. The intensity increase by a factor of 633 in combination with the fact that less than 1 out 3900 analyte molecules is likely going to be charged can further be used to provide a rough estimate for the capture efficiencies; specifically, the two numbers suggest that the capture efficiency of charged molecules may be 6 orders (considering 633* 3900) of magnitudes higher than neutral ones in the current design.

Domain 3-5 in Figure 6-3 compares the three different SERS sensor designs. Domain 4 introduces a SERS layer which is composed of localized aggregated Ag nanoparticles. Considering this layer we found no noticeable difference considering the peak intensity at 1,075 cm^{-1} yielding 191 counts which is almost identical to the value recorded using the nanolens enhanced delivery on the AgFON SERS surface layer (Domain 3). Domain 5 was used as a reference which was composed of a flat silver film underneath the nanolens array. The flat silver reference electrode showed almost no (0.2 counts) detectable peaks confirming the absence of surface enhanced plasmonic resonances in this film. Considering this set of results we conclude that the loosely aggregated Ag nanoparticle (Domain 4) is equally well suited as an enhancement layer as the AgFON standard

(Domain 3). The advantage of the loosely aggregated Ag nanoparticle (Domain 4) is that it can be deposited into desired locations and that it may enable multiplexing of various materials in further studies.

Overall the nanolens approach has the advantage that it supports a more automated analysis since it eliminates the searching and hand picking of hotspots which is a common practice in SERS related measurements. Instead, we used a standard array of detection windows outlined with the dashed lines to overcome the problems associated with the handpicking of hotspots.

6.3 Conclusion

Various nanostructured sensors currently aim to claim single molecular detection by a reduction of the active sensor size. An equally important challenge, however, can be found in the question "whether the analyte will find the nanometer sized surface". The reduction in the size of the active sensor will ultimately require research on methods which enable localized delivery. The reported electrodynamic collection concept is a first step in this direction. The process can be applied to small molecules of almost any type as long as they can be charged. The use of electrodynamic forces benefits from unique scaling laws which can be both long range using parallel plates and highly localized with sub 100 nm confinement using simple patterned insulating resists that can be charged to guide the analyte to specific locations. This is not possible with any other method. While the collection and spotting is demonstrated using surface-enhanced Raman spectroscopy the localized gas phase analyte delivery method should be applicable to other sensing concepts. The relative sensitivity increases in the case of the SERS sensor was 633 comparing the biased nanolens array with the unbiased AgFON standard. This value has not be optimized and is based on the 1 μm in diameter and 3 μm pitched hole pattern; higher values can be anticipated but would require optimization of the opening size, pitch, domain size, and domain potential. Most interesting, however, is the fact that the gas mixture contained far less charged (<1.5 ppb) analyte molecules than neutral ones (<5.9 ppm); in other words the inability to detect the neutral molecules despite the fact the concentration was 4 orders of magnitude larger than the charge molecules motivates the anticipated gains of incorporating advanced charging concepts from a sensor system

point of view. Many gas sensor systems currently use diffusion as the only mechanism of transport and dramatic improvements can be anticipated incorporating various forms of localized delivery which would impact environmental monitoring systems or the detection of chemical or biological warfare agents. One of the reported SERS domains was functionalized using Ag nanoparticles which assembled at precise locations in the photoresist openings on the basis of programmable localized precipitation. This type of localized functionalization provides an alternative to the AgFON standard. It also illustrates that the process is not only applicable to molecules. Considering the present results further it is possible to envision a multiplexed sensing platform where analytes or nanoparticles of different types are localized in an active matrix like fashion.

Chapter VII

Conclusion and Outlook

Section 1: In summary, the single reactor system that has been developed and applied in this study can be used to form charged, <10 nm sized particles (silver, tungsten, and platinum) at atmospheric pressure whereby the material can be deposited to form thick 500 nm - 2 µm deposits on selected surface areas with sub 100 nm lateral resolution in a programmable fashion. The sequence and amount of material that is extracted from the gas phase can be mixed and matched to produce multi-material deposits in desired areas on a single substrate as programmed using the external electrodes. We anticipate that the process can be extended to other metals as well as semiconductors. Little is known about atmospheric pressure deposition systems which appear to have many distinguishing features when compared to vacuum vapor phase deposition systems. This study reveals that the deposition rate can be at least a factor of 10 higher. The material can be deposited onto desired locations. No lift off is required and less material is lost. The used point source, however, has some limitation with respect to uniformity if one considers larger (>1 cm^2) samples which could be overcome by extending the process to tip arrays or orbiting substrates which has not yet been tested. Instead we decided to apply the method to identify in a combinatorial way 3D nanostructured electrode designs that improve light scattering, absorption, and minority carrier extraction of 3D bulk heterojunction photovoltaic cells. Photovoltaic cells from domains with long and dense tower arrays improve the relative power conversion efficiency by 47% when compared to flat domains on the same substrate. We have not yet changed more than a single parameter but it should be possible to test other designs where the material is varied from one domain to the next, or where structures are formed that do not simply change the pitch or height. While the interpretation of the results would be more involved than what is reported here for the nanowire based domain architecture such an approach could lead to the discovery of new designs.

Section 2: Various nanostructured sensors currently aim to claim single molecular detection by a reduction of the active sensor size. An equally important challenge, however, can be found in the question “whether the analyte will find the nanometer sized

surface". The reduction in the size of the active sensor will ultimately require research on methods which enable localized delivery. The reported electrodynamic collection concept is a first step in this direction. The process can be applied to small and large molecules of almost any type as long as they can be charged. The use of electrodynamic forces benefits from unique scaling laws which can be both long range using parallel plates and highly localized with sub 100 nm confinement using simple patterned insulating resists that can be charged to guide the analyte to specific locations. This is our view which is not possible with any other method. While the collection and spotting were demonstrated using surface-enhanced Raman spectroscopy and fluorescence based markers the localized gas phase analyte deliver method should be applicable to other sensing concepts. The relative sensitivity increases in the case of the SERS sensor was 615 comparing the biased nanolens array with the unbiased AgFON standard. The value has not be optimized and is based on the 1 μm in diameter and 3 μm pitched hole pattern shown in Figure 1; higher values can be anticipated but would require optimization of the opening size, pitch, domain size, and domain potential. Most interesting, however, is the fact that the gas mixture contained far less charged (<1.5 ppb) analyte molecules than neutral ones (<5.9 ppm); in other words the inability to detect the neutral molecules despite the fact the concentration was 4 orders of magnitude larger than the charge molecules motivates the anticipated gains of incorporating advanced charging concepts from a sensor system point of view. Many gas sensor systems currently use diffusion as the only mechanism of transport and dramatic improvements can be anticipated incorporating various forms of localized delivery which would impact environmental monitoring systems or the detection of chemical or biological warfare agents. The reported process can also be used as a programmable selected area deposition or surface treatment method with molecular ions. The sequence and amount can be mixed and matched with a lateral resolution that is several orders of magnitudes higher than what is possible using existing methods that are based on mechanical shutters or high-precision contact-printing robots. The ability to fabricate hybrid molecular arrays with control over material sequence, composition, and lateral distribution on a single substrate within a single process could potentially be used in other applications which include, proteomics and cell research, pharmaceutical screening processes, panel immunoassays, and molecular electronics[44, 45, 99].

Bibliography

1. Taton, T., C. Mirkin, and R. Letsinger, *Scanometric DNA array detection with nanoparticle probes.* Science, 2000. **289**: p. 1757-1760.
2. Jacobs, H., S. Campbell, and M. Steward, *Approaching nanoxerography: the use of electrostatic forces to position nanoparticles with 100 nm scale resolution.* Advanced Materials, 2002. **14**: p. 1553-1557.
3. Liu, W., *Nanoparticles and their biological and environmental applications.* Journal of bioscience and bioengineering, 2006. **102**: p. 1-7.
4. Pavesi, L., et al., *Optical gain in silicon nanocrystals.* Nature, 2000. **408**: p. 440-444.
5. McDonald, S., et al., *Solution-processed PbS quantum dot infrared photodetectors and photovoltaics.* Nature Materials, 2005. **4**: p. 138-142.
6. Pan, Z., Z. Dai, and Z. Wang, *Nanobelts of semiconducting oxides.* Science, 2001. **291**: p. 1947-1949.
7. Feldman, Y., et al., *High-rate, gas-phase growth of MoS2 nested inorganic fullerenes and nanotubes.* Science, 1995. **267**: p. 222-225.
8. Huang, M., et al., *Catalytic Growth of Zinc Oxide Nanowires by Vapor Transport*.* Advanced Materials, 2001. **13**: p. 113-116.
9. Morales, A. and C. Lieber, *A laser ablation method for the synthesis of crystalline semiconductor nanowires.* Science, 1998. **279**: p. 208-211.
10. Facsko, S., et al., *Formation of ordered nanoscale semiconductor dots by ion sputtering.* Science, 1999. **285**: p. 1551-1553.
11. Iijima, S., *Helical microtubules of graphitic carbon.* Nature, 1991. **354**: p. 56-58.
12. Schwyn, S., E. Garwin, and A. Schmidt-Ott, *Aerosol generation by spark discharge.* Journal of Aerosol Science, 1988. **19**: p. 639-642.
13. Camata, R., et al., *Size classification of silicon nanocrystals.* Applied Physics Letters, 1996. **68**: p. 3162-3164.
14. Akhatov, I., et al., *Aerosol focusing in micro-capillaries: Theory and experiment.* Journal of Aerosol Science, 2008. **39**(8): p. 691-709.
15. Di Fonzo, F., et al., *Focused nanoparticle-beam deposition of patterned microstructures.* Applied Physics Letters, 2000. **77**: p. 910.
16. Barry, C., et al., *Printing nanoparticles from the liquid and gas phases using nanoxerography.* Nanotechnology, 2003. **14**: p. 1057.
17. Zonnevylle, A., et al., *Directed assembly of nano-particles with the help of charge patterns created with scanning electron microscope.* Microelectronic Engineering, 2009. **86**: p. 803-805.
18. Barry, C.R., et al., *Printing nanoparticle building blocks from the gas phase using nanoxerography.* Applied Physics Letters, 2003. **83**(26): p. 5527-5529.
19. Barry, C.R., J. Gu, and H.O. Jacobs, *Charging Process and Coulomb-Force-Directed Printing of Nanoparticles with Sub-100-nm Lateral Resolution.* Nano Letters, 2005. **5**(10): p. 2078-2084.
20. Barry, C.R. and H.O. Jacobs, *Fringing field directed assembly of nanomaterials.* Nano Letters, 2006. **6**(12): p. 2790-2796.

21. Cole, J., et al., *Continuous nanoparticle generation and assembly by atmospheric pressure arc discharge.* Applied Physics Letters, 2009. **95**: p. 113101.
22. Cole, J.J., et al., *Mimicking Electrodeposition in the Gas Phase: A Programmable Concept for Selected-Area Fabrication of Multimaterial Nanostructures.* Small, 2010. **6**(10): p. 1117-1124.
23. Lin, E.C., J.J. Cole, and H.O. Jacobs, *Gas phase electrodeposition: a programmable multimaterial deposition method for combinatorial nanostructured device discovery.* Nano Letters, 2010. **10**(11): p. 4494-4500.
24. Schmitz, C., M. Thelakkat, and H. Schmidt, *A combinatorial study of the dependence of organic LED characteristics on layer thickness.* Advanced Materials, 1999. **11**: p. 821-826.
25. Sun, T. and G. Jabbour, *Combinatorial screening and optimization of luminescent materials and organic light-emitting devices.* MRS Bulletin, 2002. **27**: p. 309-315.
26. Godovsky, D., et al., *The use of combinatorial materials development for polymer solar cells.* Advanced Materials for Optics and Electronics, 2000. **10**: p. 47-54.
27. Haber, J., et al. *Combinatorial discovery of new thin film photovoltaics*. in *Thirty-First IEEE Photovoltaic Specialists Conference,*. 2005. Lake Buena Vista, FL, USA.
28. Kolla, P., *Gas chromatography, liquid chromatography and ion chromatography adapted to the trace analysis of explosives.* Journal of Chromatography A, 1994. **674**(1-2): p. 309-318.
29. Tuovinen, K., H. Paakkanen, and O. Hänninen, *Determination of soman and VX degradation products by an aspiration ion mobility spectrometry.* Analytica chimica acta, 2001. **440**(2): p. 151-159.
30. Ewing, R.G., et al., *A critical review of ion mobility spectrometry for the detection of explosives and explosive related compounds.* Talanta, 2001. **54**(3): p. 515-529.
31. Fenn, J.B., et al., *Electrospray ionization for mass spectrometry of large biomolecules.* Science, 1989. **246**(4926): p. 64-71.
32. Comini, E., *Metal oxide nano-crystals for gas sensing.* Analytica chimica acta, 2006. **568**(1): p. 28-40.
33. Comini, E., et al., *Stable and highly sensitive gas sensors based on semiconducting oxide nanobelts.* Applied Physics Letters, 2002. **81**: p. 1869.
34. Kong, J., et al., *Nanotube molecular wires as chemical sensors.* Science, 2000. **287**(5453): p. 622-625.
35. Arnold, M.S., et al., *Field-effect transistors based on single semiconducting oxide nanobelts.* The Journal of Physical Chemistry B, 2003. **107**(3): p. 659-663.
36. Li, M., H. Tang, and M. Roukes, *Ultra-sensitive NEMS-based cantilevers for sensing, scanned probe and very high-frequency applications.* Nature Nanotechnology, 2007. **2**(2): p. 114-120.
37. Werle, P., et al., *Near-and mid-infrared laser-optical sensors for gas analysis.* Optics and Lasers in Engineering, 2002. **37**(2): p. 101-114.
38. Biggs, K.B., et al., *Surface-Enhanced Raman Spectroscopy of Benzenethiol Adsorbed from the Gas Phase onto Silver Film over Nanosphere Surfaces: Determination of the Sticking Probability and Detection Limit Time.* The Journal of Physical Chemistry A, 2009. **113**(16): p. 4581-4586.

39. Piorek, B.D., et al., *Free-surface microfluidic control of surface-enhanced Raman spectroscopy for the optimized detection of airborne molecules.* Proceedings of the National Academy of Sciences, 2007. **104**(48): p. 18898.
40. Schedin, F., et al., *Detection of individual gas molecules adsorbed on graphene.* Nature Materials, 2007. **6**(9): p. 652-655.
41. Hill, H.H. and S.J. Martin, *Conventional analytical methods for chemical warfare agents.* Pure and applied chemistry, 2002. **74**(12): p. 2281-2292.
42. Fodor, S.P., et al., *Light-directed, spatially addressable parallel chemical synthesis.* Science, 1991. **251**(4995): p. 767-773.
43. Dulcey, C.S., et al., *Deep UV photochemistry of chemisorbed monolayers: patterned coplanar molecular assemblies.* Science, 1991. **252**(5005): p. 551-554.
44. MacBeath, G. and S.L. Schreiber, *Printing proteins as microarrays for high-throughput function determination.* Science, 2000. **289**(5485): p. 1760-1763.
45. Schena, M., et al., *Parallel human genome analysis: microarray-based expression monitoring of 1000 genes.* Proceedings of the National Academy of Sciences, 1996. **93**(20): p. 10614.
46. Dick, L.A., et al., *Metal film over nanosphere (MFON) electrodes for surface-enhanced Raman spectroscopy (SERS): Improvements in surface nanostructure stability and suppression of irreversible loss.* The Journal of Physical Chemistry B, 2002. **106**(4): p. 853-860.
47. Jang, K.-J. and J.-M. Nam, *Direct-write nanoparticle microarrays for cell assays.* Small, 2008. **4**(11): p. 1930-1935.
48. Barry, R.A., III, et al., *Direct-Write Assembly of 3D Hydrogel Scaffolds for Guided Cell Growth.* Advanced Materials (Weinheim, Germany), 2009. **21**(23): p. 2407-2410.
49. Gratson, G.M., et al., *Direct-write assembly of three-dimensional photonic crystals: conversion of polymer scaffolds to silicon hollow-woodpile structures.* Advanced Materials (Weinheim, Germany), 2006. **18**(4): p. 461-465.
50. Meitl, M.A., et al., *Transfer printing by kinetic control of adhesion to an elastomeric stamp.* Nature Materials, 2006. **5**(1): p. 33-38.
51. Kravchenko, T.A., et al., *The influence of the ion-exchange groups nature and the degree of chemical activation by silver on the process of copper electrodeposition into the ion exchanger.* Electrochimica Acta, 2007. **53**(2): p. 330-336.
52. Sun, M., et al., *Electrodeposition of highly uniform magnetic nanoparticle arrays in ordered alumite.* Applied Physics Letters, 2001. **78**(19): p. 2964-2966.
53. Bera, D., et al., *Palladium nanoparticle arrays using template-assisted electrodeposition.* Applied Physics Letters, 2003. **82**(18): p. 3089-3091.
54. Ohgai, T., et al., *Magneto-sensitive nickel nanowires fabricated by electrodeposition into multi- and single-ion track templates.* Journal of Applied Electrochemistry, 2006. **36**(10): p. 1157-1162.
55. Jaworek, A., A. Krupa, and T. Czech, *Modern electrostatic devices and methods for exhaust gas cleaning: A brief review.* Journal of Electrostatics, 2006. **65**(3): p. 133-155.
56. Kraetschmer, W., et al., *Solid C60: a new form of carbon.* Nature (London, United Kingdom), 1990. **347**(6291): p. 354-8.

57. Iijima, S., *Helical microtubules of graphitic carbon.* Nature (London, United Kingdom), 1991. **354**(6348): p. 56-8.
58. Ebbesen, T.W. and P.M. Ajayan, *Large-scale synthesis of carbon nanotubes.* Nature (London, United Kingdom), 1992. **358**(6383): p. 220-2.
59. Journet, C., et al., *Large-scale production of single-walled carbon nanotubes by the electric-arc technique.* Nature (London), 1997. **388**(6644): p. 756-758.
60. Han, W., et al., *Synthesis of GaN-carbon composite nanotubes and GaN nano-rods by arc discharge in nitrogen atmosphere.* Applied Physics Letters, 2000. **76**(5): p. 652-654.
61. Bera, D., et al., *In-situ synthesis of palladium nanoparticles-filled carbon nanotubes using arc-discharge in solution.* Chemical Physics Letters, 2004. **386**(4-6): p. 364-368.
62. Liu, S.-M., et al., *Synthesis of silicon nanowires and nanoparticles by arc-discharge in water.* Chemical Communications (Cambridge, United Kingdom), 2005(37): p. 4690-4692.
63. Tsai, D.H., et al., *Electrostatic-directed deposition of nanoparticles on a field generating substrate.* Nanotechnology, 2005. **16**(9): p. 1856-1862.
64. Characteristic spectral emission from pure Ar discharges includes red-purple emission peaks at 697nm due to ionization of Ar molecules into Ar+ and 481nm for Ar++, while blue-white O2 discharges contain ionized peaks at 419nm due to O2+ and 646 and 777nm due to the dissociation of the O2 molecule into atomic O. The noble gases that we used to provide an inert environment discussed later (Ar, He) show similar basic arc characteristics and are also known to release electrons by charging to a positively ionized state.
65. Smirnov, B.M., *Physics of Ionized Gases*, ed. H.R. Reiss. 2001, New York: John Wiley & Sons, Inc. 381.
66. High current 100A arc discharges classically referred to as high temperature thermal plasmas or plasma sprays describe a case where the electrons and ions are in thermal equilibrium and sufficiently hot to quickly evaporate the cathode material. However, erosion and the production of nanoparticles has been reported even under corona discharge conditions which sustain much smaller currents, typically less than 500 μA. The input power that we used in the experiments reported here ranged between 1-100W with controlled arc currents of less than 100mA which is quite similar to what is used in atmospheric pressure arc discharge lamps. We anticipate that higher current levels are likely going to work as well.
67. Considering that nanoparticles originate from the grounded cathode and do not deposit on insulating surfaces leads to the conclusions that Coulomb forces dominate the deposition process and that nanoparticles charge to be unipolar prior to deposition on the sample electrode. If neutral particles were present they would coat the insulating surfaces and this is not the case. If the aerosol were to have both positive and negatively charged particles above the sample surface we would again anticipate that the insulating surface would build up a particle layer, contrary to observation. The material flux forming the deposits (F,G) together with the recorded positive ion current and absence of deposition on the insulting surfaces can only be explained if the nanomaterials are predominantly positively

charged. Insulating surfaces are initially uncharged and we would expect a limited amount of charged material to deposit until the insulator fully charges. Such deposition is not observed within the ~5 nm resolution limit of our SEM. This behavior can be explained if we consider the higher mobility of gas ions when compared to nanoparticles. Gas ions such as Ar+ in Figure 3 are likely going to be responsible for establishing an equilibrium charge and potential distribution as the experiment is started. As indicated in Figure 3C Ar+ surrounding the insulator is expected to be responsible for preventing deposition of the positively charged M+ nanoparticles on the insulator.

68. Dabringhausen, L., et al., *Determination of HID electrode falls in a model lamp I: pyrometric measurements.* Journal of Physics D: Applied Physics, 2002. **35**(14): p. 1621-1630.
69. Luhmann, J., et al., *Determination of HID electrode falls in a model lamp II: langmuir-probe measurements.* Journal of Physics D: Applied Physics, 2002. **35**(14): p. 1631-1638.
70. Hinds, W.C., *Aerosol Technology*. 2nd ed. 1999, New York: John Wiley & Sons, Inc. 483.
71. Fridman, A. and L.A. Kennedy, *Plasma Physics and Engineering*. 2004, New York: Taylor & Francis Books, Inc. 853.
72. The competition between neighboring areas attracting materials within the Debye radius could in principle affect the deposition rate. However, we have not been able to increase the deposition rate going from a dense pattern to an isolated line which suggests that diffusion plays a role in the observed uniformity.
73. Romay, F.J., B.Y.H. Liu, and D.Y.H. Pui, *A sonic jet corona ionizer for electrostatic discharge and aerosol neutralization.* Aerosol Science and Technology, 1994. **20**(1): p. 31-41.
74. Aleksandrov, N. and E. Bazelyan, *Simulation of long-streamer propagation in air at atmospheric pressure.* Journal of Physics D: Applied Physics, 1996. **29**: p. 740-752.
75. Aleksandrov, N. and E. Bazelyan, *Ionization processes in spark discharge plasmas.* Plasma Sources Science and Technology, 1999. **8**: p. 285-294.
76. Rodrfguez, A., et al., *An air breakdown kinetic model.* Journal of Applied Physics, 1991. **70**: p. 2015-2022.
77. Mor, G., et al., *High efficiency double heterojunction polymer photovoltaic cells using highly ordered TiO nanotube arrays.* Applied Physics Letters, 2007. **91**: p. 152111.
78. Brabec, C.J., et al., *Origin of the Open Circuit Voltage of Plastic Solar Cells.* Advanced Functional Materials, 2001. **11**: p. 374-380.
79. Roman, L., et al., *Trapping light in polymer photodiodes with soft embossed gratings.* Advanced Materials, 2000. **12**: p. 189-195.
80. Na, S., et al., *Surface relief gratings on poly (3-hexylthiophene) and fullerene blends for efficient organic solar cells.* Applied Physics Letters, 2007. **91**: p. 173509.
81. Kayes, B., H. Atwater, and N. Lewis, *Comparison of the device physics principles of planar and radial pn junction nanorod solar cells.* Journal of Applied Physics, 2005. **97**: p. 114302.

82. Ma, W., et al., *Thermally stable, efficient polymer solar cells with nanoscale control of the interpenetrating network morphology.* Advanced Functional Materials, 2005. **15**: p. 1617-1622.
83. Park, S., et al., *Bulk heterojunction solar cells with internal quantum efficiency approaching 100&percnt.* Nature Photonics, 2009. **3**: p. 297-302.
84. Reyes-Reyes, M., et al., *Meso-structure formation for enhanced organic photovoltaic cells.* Org. Lett, 2005. **7**: p. 5749-5752.
85. Janata, J. and M. Josowicz, *Conducting polymers in electronic chemical sensors.* Nature Materials, 2003. **2**(1): p. 19-24.
86. Yamazoe, N. and N. Miura, *Environmental gas sensing.* Sensors and Actuators B: Chemical, 1994. **20**(2-3): p. 95-102.
87. Sheehan, P.E. and L.J. Whitman, *Detection limits for nanoscale biosensors.* Nano Letters, 2005. **5**(4): p. 803-807.
88. Lee, H., et al., *Three-dimensional assembly of nanoparticles from charged aerosols.* Nano Letters, 2011. **11**(1): p. 119-124.
89. Weekes, S.M., et al., *Macroscopic arrays of magnetic nanostructures from self-assembled nanosphere templates.* Langmuir, 2007. **23**(3): p. 1057-1060.
90. Kao, P., et al., *Surface-Enhanced Raman Detection on Metalized Nanostructured Poly (p-xylylene) Films.* Advanced Materials, 2008. **20**(18): p. 3562-3565.
91. Steiner, W.E., et al., *Rapid screening of aqueous chemical warfare agent degradation products: ambient pressure ion mobility mass spectrometry.* Analytical Chemistry, 2002. **74**(17): p. 4343-4352.
92. Valentine, S.J., et al., *Toward plasma proteome profiling with ion mobility-mass spectrometry.* Journal of proteome research, 2006. **5**(11): p. 2977-2984.
93. Cloupeau, M. and B. Prunet-Foch, *Electrohydrodynamic spraying functioning modes: a critical review.* Journal of Aerosol Science, 1994. **25**(6): p. 1021-1036.
94. Ganan-Calvo, A., J. Davila, and A. Barrero, *Current and droplet size in the electrospraying of liquids. Scaling laws.* Journal of Aerosol Science, 1997. **28**(2): p. 249-275.
95. Cloupeau, M. and B. Prunet-Foch, *Electrostatic spraying of liquids in cone-jet mode.* Journal of Electrostatics, 1989. **22**(2): p. 135-159.
96. Hiraoka, K., K. Murata, and I. Kudaka, *Species-selectivity effects in the production of electrospray ions.* Rapid communications in mass spectrometry, 1993. **7**(5): p. 363-373.
97. Koo, T.W., et al., *Specific chemical effects on surface-enhanced Raman spectroscopy for ultra-sensitive detection of biological molecules.* Applied spectroscopy, 2004. **58**(12): p. 1401-1407.
98. Woo, C.G., et al., *Selective Nanopatterning of Protein via Ion-Induced Focusing and its Application to Metal-Enhanced Fluorescence.* Small, 2011. **7**(13): p. 1790-1794.
99. Kanea, R.S., et al., *Patterning proteins and cells using soft lithography.* The Biomaterials Silver Jubilee Compendium: The Best Papers Published in Biomaterials, 1980-2004, 2007: p. 161.